



# A detailed microkinetic model for diesel engine emissions oxidation on platinum based diesel oxidation catalysts (DOC)

Hom Sharma, Ashish Mhadeshwar\*

Department of Chemical, Materials, and Biomolecular Engineering and Center for Clean Energy Engineering, University of Connecticut, 191 Auditorium Road, Unit 3222, Storrs, CT 06269, United States

## ARTICLE INFO

### Article history:

Received 13 June 2012

Received in revised form 17 August 2012

Accepted 21 August 2012

Available online 30 August 2012

### Keywords:

Emissions

Oxidation

Platinum

Microkinetic

Diesel

DOC

Aftertreatment

## ABSTRACT

In this work, a comprehensive 124-step (62 reversible) microkinetic model is developed for the oxidation of five major diesel engine emission components (carbon monoxide, nitric oxide, formaldehyde, ammonia, and hydrogen cyanide) on Pt. Kinetic parameters for the detailed microkinetic model are extracted from ultra-high vacuum (UHV) temperature programmed desorption/reaction (TPD/TPR) experiments in literature. Starting with these kinetic parameters as initial estimates, the surface reaction mechanism is extensively tested against practically more relevant operating conditions, such as atmospheric pressure, dilute emissions concentrations, and short residence times, typically experienced by the Diesel Oxidation Catalysts (DOCs). In each of the five oxidation cases, mechanistic analysis is presented to uncover the most important reaction chemistry. The microkinetic model shows very good agreement with multiple experimental data sets on monolith and fixed bed reactor scale, for the oxidation of all five components. For practical implementation, the mechanism is further reduced to 94 steps (47 reversible) using preliminary model reduction.

© 2012 Elsevier B.V. All rights reserved.

## 1. Introduction

Today's world consumes ~87 million barrels of fossil fuel/oil every day [1], of which more than 20% is consumed in the US [2]. Almost all the freight locomotives and 75% of the commercial marine vessels in the US are powered by diesel [3]. Given the large consumption of diesel in the US, emissions from the diesel engine exhaust pose a major concern for human health, global warming, and environmental pollution. According to a US-based study by the Clean Air Task Force, toxic emissions from diesel engine exhaust claim 21,000 lives per year due to respiratory and cardiovascular diseases (~3,000 from lung cancer), result in 27,000 heart attacks and 400,000 asthma attacks per year, lead to ~\$139 billion in monetized damages or losses per year, and cause an enormous threat to the environment [4,5]. Various toxic emissions in diesel exhaust include, but are not limited to, carbon monoxide (CO), carbon dioxide (CO<sub>2</sub>), nitrogen oxides (NO<sub>x</sub>), sulfur oxides (SO<sub>x</sub>), volatile organic compounds (VOCs) [6], poly aromatic hydrocarbons (PAHs) [7,8], and particulate matter (PM) [9]. A number of secondary nitrogen-containing emissions such as hydrogen cyanide (HCN) and ammonia (NH<sub>3</sub>) as well as aldehydes such as formaldehyde (CH<sub>2</sub>O) and acetaldehyde (CH<sub>3</sub>CHO) have been observed in the untreated or treated exhaust [10–14].

Platinum (Pt)/Palladium (Pd)-based Diesel Oxidation Catalysts (DOCs) represent the most predominant technology to oxidize such emissions from the exhaust [15]. DOCs are often coupled with other aftertreatment components such as Selective Catalytic Reduction (SCR) and Diesel Particulate Filter (DPF) [16]. For urea-SCR of NO<sub>x</sub>, an upstream DOC (see Fig. 1a) is required to oxidize some NO to NO<sub>2</sub>, since the highest rates are attained with an equimolar ratio of NO and NO<sub>2</sub> [17]. In DPFs, NO<sub>2</sub> can also be used to oxidize the accumulated soot [18–20]. For hydrocarbon (HC)-SCR of NO<sub>x</sub>, a DOC is needed downstream (see Fig. 1b) to oxidize the SCR byproducts, such as HCN, CO, NH<sub>3</sub>, CH<sub>2</sub>O, acetonitrile (CH<sub>3</sub>CN), and CH<sub>3</sub>CHO, to relatively 'less' harmful CO<sub>2</sub>, H<sub>2</sub>O, and NO<sub>x</sub>. DOCs are also used in natural gas-based stationary power generation (gas turbines) to oxidize CO [21–23]. A robust emissions control system requires integration of multiple aftertreatment units, which in turn requires a complete understanding of the chemical reactions taking place inside those units.

In this work, we focus on developing a detailed mechanistic understanding of the catalytic reaction kinetics for the oxidation of five major emissions on Pt-based DOCs. The five chemistries include oxidation of CO, NO, CH<sub>2</sub>O, NH<sub>3</sub>, and HCN (see Table 1). Even though CO and NO oxidation chemistries are well studied [24–36], this work presents the *first comprehensive reaction mechanism for a Pt-based DOC* that can be used to predict the *oxidation behavior of five key primary or secondary emissions*. The paper is organized as follows. First, we discuss the methodology for the development of emissions oxidation chemistry in Section 2. In Section 3, we discuss

\* Corresponding author. Tel.: +1 443 523 8609; fax: +1 860 486 2959.

E-mail address: [ashish.mhadeshwar@gmail.com](mailto:ashish.mhadeshwar@gmail.com) (A. Mhadeshwar).

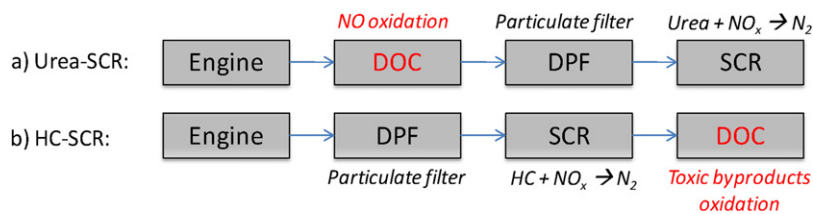


**Fig. 1.** Role of DOC in toxic emissions oxidation from diesel engine exhaust. The representative configurations focused around (a) Urea-SCR and (b) HC-SCR illustrate the importance of DOC in both cases.

the estimation of kinetic parameters from ultra-high vacuum (UHV) temperature programmed desorption/reaction (TPD/TPR) experiments in literature. Performance of the reaction mechanism is demonstrated in Section 4 at practically more relevant operating conditions. Preliminary mechanism reduction is discussed in Section 5. Finally, we discuss the overall limitations of this work in Section 6, followed by conclusions.

## 2. Emissions oxidation chemistry development

The overall approach for the development of a comprehensive microkinetic model for the oxidation of five emissions consists of three major steps. First, an elementary step reaction mechanism is proposed for the oxidation of each of the five emissions. Second, the kinetic parameters associated with various species and reactions are extracted from literature surface science experiments or estimated from theory. Finally, the surface reaction mechanism, combined with reactor modeling, is validated against multiple monolith and fixed bed experiments conducted in practically more relevant operating conditions such as dilute emissions concentrations, atmospheric pressure, and short residence times.

### 2.1. Development of the surface reaction mechanism

Elementary surface reactions for the oxidation of CO, NO, NH<sub>3</sub>, HCN, and CH<sub>2</sub>O on Pt are shown in Appendix A (Table S1) of the supplementary material. The complete oxidation products include CO<sub>2</sub>, NO<sub>2</sub>, and H<sub>2</sub>O, whereas the incomplete oxidation products include CO, NO, and N<sub>2</sub>O. Additional stable species, such as O<sub>2</sub>, N<sub>2</sub>, H<sub>2</sub>, and C<sub>2</sub>N<sub>2</sub> (cyanogen), as well as intermediates such as, C, H, OH, COOH, N, NH, NH<sub>2</sub>, CN, and HCO, are also considered. Inclusion of various cross-interactive reaction pathways, such as (i) CO and H<sub>2</sub> oxidation, (ii) NO and H<sub>2</sub> oxidation, (iii) CO oxidation and carbon formation/oxidation, and (iv) HCN oxidation and C<sub>2</sub>N<sub>2</sub> formation, is a unique and novel feature of this comprehensive mechanism. The overall reaction mechanism consists of 21 surface species and 124 irreversible surface reactions (62 reversible pairs).

### 2.2. Methodology for kinetic parameter extraction/estimation

Binding energies and activation energies in the surface reaction mechanism are extracted from UHV temperature programmed surface science experiments in literature, estimated using the semi-empirical Unity Bond Index-Quadratic Exponential Potential (UBI-QEP) method [37,38], or taken from first principles quantum

mechanical Density Functional Theory (DFT) calculations in literature. For each stable species in the reaction mechanism, we have considered multiple TPD experimental data on Pt facets to extract the species binding energies ( $Q$ ) and adsorbate-adsorbate interactions ( $\alpha$ ). Resulting parameters from the TPD simulations are shown in Table 2. Detailed information about the experimental conditions and the experimental vs. model predicted peak temperatures is given in Section 3.1. Similarly, various TPR experimental data sets in the literature are used to extract the activation energies ( $E_a$ ) and bond indices (BI) for the emissions oxidation reactions. Details of the TPR simulations are discussed in Section 3.2. The semi-empirical UBI-QEP method is used to estimate the coverage dependent activation energies on-the-fly in these simulations. Functional forms to compute the activation energies are given in Appendix B of the supplementary material. Some of the parameters, especially the adsorbate-adsorbate interactions (e.g., NO<sup>\*</sup>-O<sup>\*</sup>, OH<sup>\*</sup>-O<sup>\*</sup>), are taken from literature data. Pre-exponential factors are taken as initial estimates based on Transition State Theory (TST), e.g., 10<sup>13</sup> s<sup>-1</sup> for desorption and 10<sup>11</sup> s<sup>-1</sup> for Langmuir-Hinshelwood type surface reactions [39]. As Pt(111) is one of the most stable facets among all facets of Pt, site density ( $\sigma$ ) of 1.5 × 10<sup>15</sup> sites/cm<sup>2</sup> (2.5 × 10<sup>-9</sup> mol/cm<sup>2</sup>) is used in the simulations based on the typical estimate for the Pt(111) facet [40].

### 2.3. Mechanism performance and validation at more realistic conditions

In practically more realistic situations, the operating conditions experienced by the DOCs are significantly different from the UHV conditions for temperature programmed experiments or the zero-temperature conditions used in first principles calculations. Therefore, it is important to ensure that the microkinetic model developed with such parameters also works in the practically more relevant conditions, such as atmospheric pressure, dilute emissions concentrations (few tens to hundreds of ppm), and short residence times. Fixed bed and monolith scale experimental data reported in the literature as well as in our experiments are used to check the microkinetic model performance. Details of the mechanism performance and analysis of reaction paths are presented in Section 4.

Gas phase chemistry is taken into account through the GRI-Mech 3.0 reaction mechanism [41]. Species thermodynamic data are taken from the GRI thermodynamic database. For C<sub>2</sub>N<sub>2</sub>, the thermodynamic database in ChemKin format is derived in Appendix C of the supplementary material.

## 3. Parameter estimation from UHV experiments

As mentioned previously, UHV-TPD simulations of various species are carried out to extract the species binding energies and adsorbate-adsorbate interactions (see Table 2). Similarly, UHV-TPR simulations are carried out for various systems to extract the bond indices (related to activation energies). First, we discuss representative TPD simulations, and follow up with the TPR

**Table 1**

Overall chemistry for the oxidation of engine exhaust emissions.

Emission component	Chemistry
CO	CO + ½O <sub>2</sub> → CO <sub>2</sub>
NO	NO + ½O <sub>2</sub> → NO <sub>2</sub>
CH <sub>2</sub> O	CH <sub>2</sub> O + O <sub>2</sub> → CO, CO <sub>2</sub> , H <sub>2</sub> , and H <sub>2</sub> O
NH <sub>3</sub>	NH <sub>3</sub> + O <sub>2</sub> → NO, NO <sub>2</sub> , N <sub>2</sub> O, N <sub>2</sub> , H <sub>2</sub> , and H <sub>2</sub> O
HCN	HCN + O <sub>2</sub> → CO, CO <sub>2</sub> , NO, NO <sub>2</sub> , N <sub>2</sub> O, C <sub>2</sub> N <sub>2</sub> , H <sub>2</sub> , and H <sub>2</sub> O

**Table 2**

List of species binding energies (or activation energies for associative desorption) and adsorbate interactions extracted from various TPD simulations (see Section 3.1 for details of the TPD simulations). If the extracted adsorbate interactions are insignificant based on the experiments at multiple initial coverages, they are explicitly indicated with zeros (for NO<sub>2</sub>, HCN, and C<sub>2</sub>N<sub>2</sub>).

Species	Q or E [kcal/mol]	Catalyst and reference	Q or E range from literature [kcal/mol]
O <sub>2</sub> (associative desorption)	49.5–34θ <sub>O</sub>	Pt(1 1 1) [127]	40–60 [32,116,127–129]
	55–29θ <sub>O</sub>	Pt(1 1 1) [130]	
	52.6–34θ <sub>O</sub>	Pt(1 1 1) [116]	
CO	36–6.1θ <sub>CO</sub>	Pt(1 0 0) [79]	29–54 [32,42–47,118]
	34.9–7.5θ <sub>CO</sub>	Pt(1 1 1) [131]	
	37–7.7θ <sub>CO</sub>	Pt(1 1 1) [25]	
	35.8–12θ <sub>CO</sub>	Pt(1 1 1) [132]	
H <sub>2</sub> (associative desorption)	21–5θ <sub>H</sub>	Pt(1 1 1) [133]	13–34 [65,66,82,122,124,133–136]
	19.8–2.5θ <sub>H</sub>	Pt(1 1 1) [137]	
H <sub>2</sub> O	11.4 – 2.8θ <sub>H<sub>2</sub>O</sub>	Pt(1 1 1) [79]	6–15 [79,115,121,134,138–141]
	10.9 – 1.9θ <sub>H<sub>2</sub>O</sub>	Pt(1 1 1) [80]	
NH <sub>3</sub>	20.7 – 9.9θ <sub>NH<sub>3</sub></sub>	Pt(1 1 1) [142]	14–23 [51–56,83,85,143]
	21.2 – 10θ <sub>NH<sub>3</sub></sub>	Pt(1 1 1) [144]	
	20.1 – 8.8θ <sub>NH<sub>3</sub></sub>	Pt(1 1 1) [78]	
NO	29.5–9.7θ <sub>NO</sub>	Pt(1 1 1) [40]	18–43 [33–35,49,53,59,62]
	29.8–7.6θ <sub>NO</sub>	Pt(1 1 1) [145]	
	28.4–6.8θ <sub>NO</sub>	Pt(1 1 1) [146]	
NO <sub>2</sub>	19 – 0θ <sub>NO<sub>2</sub></sub>	Pt(1 1 1) [58]	17–38 [57–63]
HCN	26.1–0θ <sub>HCN</sub>	Pt(1 1 2) [67]	14–30 [53,68]
	16.6	Pt(1 1 1) [147]	
CH <sub>2</sub> O	14.7	Pt(1 1 1) [77]	11–16 [65,124]
C <sub>2</sub> N <sub>2</sub>	21	Pt(1 1 1) [70]	12–42 [148,149]
	22.3 – 0θ <sub>C<sub>2</sub>N<sub>2</sub></sub>	Pt(1 1 1) [71]	
	19.7	Pt(1 1 1) [72]	

simulations, along with reaction path analysis (RPA) to provide mechanistic insights.

### 3.1. UHV-TPD simulations

In this work, we have studied desorption of multiple species included in the reaction mechanism. For each species, multiple TPD data sets (>25 experimental data sets in total) on Pt surface are used to extract species binding energies and adsorbate–adsorbate interactions (see Fig. 2 for a few representative TPD simulations and comparison to experimental data). All desorption rates are shown in mol/cm<sup>2</sup>/s, but turn-over frequencies (s<sup>-1</sup>) can be obtained by dividing with the site density (mol/cm<sup>2</sup>). Extracted kinetic parameters from the TPD simulations are given in Table 2. Even though this analysis is fairly straightforward, next we briefly discuss a few important parameters and features.

From multiple CO TPD experiments (see Fig. 2a for an example), we have extracted Q<sub>CO</sub> (35–37 kcal/mol) and CO<sup>\*</sup>–CO<sup>\*</sup> adsorbate interactions (6–12 kcal/mol/ML). Our estimates are within the reported heat of CO chemisorption range of 29–54 kcal/mol [29,42–47]. We note that the binding energies and adsorbate interactions for the CO oxidation chemistry are similar to the ones reported by Mhadeshwar and Vlachos [29]. The extracted Q<sub>NO</sub> based on multiple NO TPD experiments (see Fig. 2b for an example) is in the range of 28–30 kcal/mol with NO<sup>\*</sup>–NO<sup>\*</sup> adsorbate interactions of 6–10 kcal/mol/ML. These estimates are well aligned with the reported Q<sub>NO</sub> (18–43 kcal/mol [33,35,48,49]). Based on the work of Hauptmann et al., Q<sub>NO</sub> depends on the O<sup>\*</sup> coverage as well; and these repulsive interactions are taken as 16 kcal/mol/ML [34]. The H<sup>\*</sup>–H<sup>\*</sup> adsorbate interactions are small (1.9 kcal/mol/ML), as seen from the relatively smaller shift in peak temperatures (see Fig. 2c). O<sup>\*</sup>–O<sup>\*</sup> adsorbate interactions of 13.3 kcal/mol/ML are taken from the literature [34] and are also consistent with our TPD simulations shown in Fig. 2d. Based on our TPD simulations (not shown), the estimated Q<sub>NH<sub>3</sub></sub> of 20–22 kcal/mol is also within the reported

range of 14–23 kcal/mol [50–56]. Based on the peak shift with initial coverage, the NH<sub>3</sub><sup>\*</sup>–NH<sub>3</sub><sup>\*</sup> adsorbate interactions are estimated to be 9.5 kcal/mol/ML. Q<sub>NO<sub>2</sub></sub> is estimated to be 19 kcal/mol, which is consistent with literature estimates of 17–38 kcal/mol [57–63]; but no significant adsorbate interactions are observed in the experimental data [58] and the TPD simulations (see Fig. 2e). Q<sub>CH<sub>2</sub>O</sub> is estimated as 14.7 kcal/mol (not shown), which is consistent with the reported range of 11–16 kcal/mol [64–66].

Compared to other species, the TPD behavior of HCN is different (see Fig. 2f), as it shows decomposition and formation of H<sub>2</sub> and C<sub>2</sub>N<sub>2</sub> as products along with typical HCN desorption. From TPD experiments [67], Q<sub>HCN</sub> is estimated to be 26.1 kcal/mol. This is consistent with the literature reported range of 14–30 kcal/mol [53,68]. Experimental data suggest that desorption of HCN from Pt is independent of the surface coverage, i.e., the adsorbate interactions are insignificant [69]. Q<sub>C<sub>2</sub>N<sub>2</sub></sub><sup>avg</sup> is estimated to be 21 kcal/mol from the TPD simulations of C<sub>2</sub>N<sub>2</sub> on Pt(1 1 1) surface [70–72]. To correctly capture the peak location of C<sub>2</sub>N<sub>2</sub> formation from the HCN TPD (670 K), bond index of the reaction pair R<sub>123</sub>–R<sub>124</sub>: C<sub>2</sub>N<sub>2</sub><sup>+</sup>\* ↔ 2CN<sup>\*</sup> is modified to 0.73 (starting from 0.5). With this modification, our model shows good agreement with the peak locations for all three products (HCN, H<sub>2</sub>, and C<sub>2</sub>N<sub>2</sub>), as shown in Fig. 2f.

These and many other kinetic parameters estimated from the UHV-TPD simulations (see Table 2) form the basis of the UHV-TPR simulations described next, and also of the fixed bed and monolith simulations described in Section 4.

### 3.2. UHV-TPR simulations

#### 3.2.1. CO oxidation

Fig. 3a shows the peaks for CO<sub>2</sub> formation rate and excess CO desorption rate from the CO oxidation UHV-TPR experiments on Pt(1 1 1) by Gerrard et al. [26]. Initial coverages include 0.29 ML of CO<sup>\*</sup> and 0.25 ML of O<sup>\*</sup>. As CO<sup>\*</sup> oxidation to CO<sub>2</sub><sup>\*</sup> (R<sub>10</sub>) is the most important reaction, bond index of that reaction pair R<sub>9</sub>–R<sub>10</sub>:

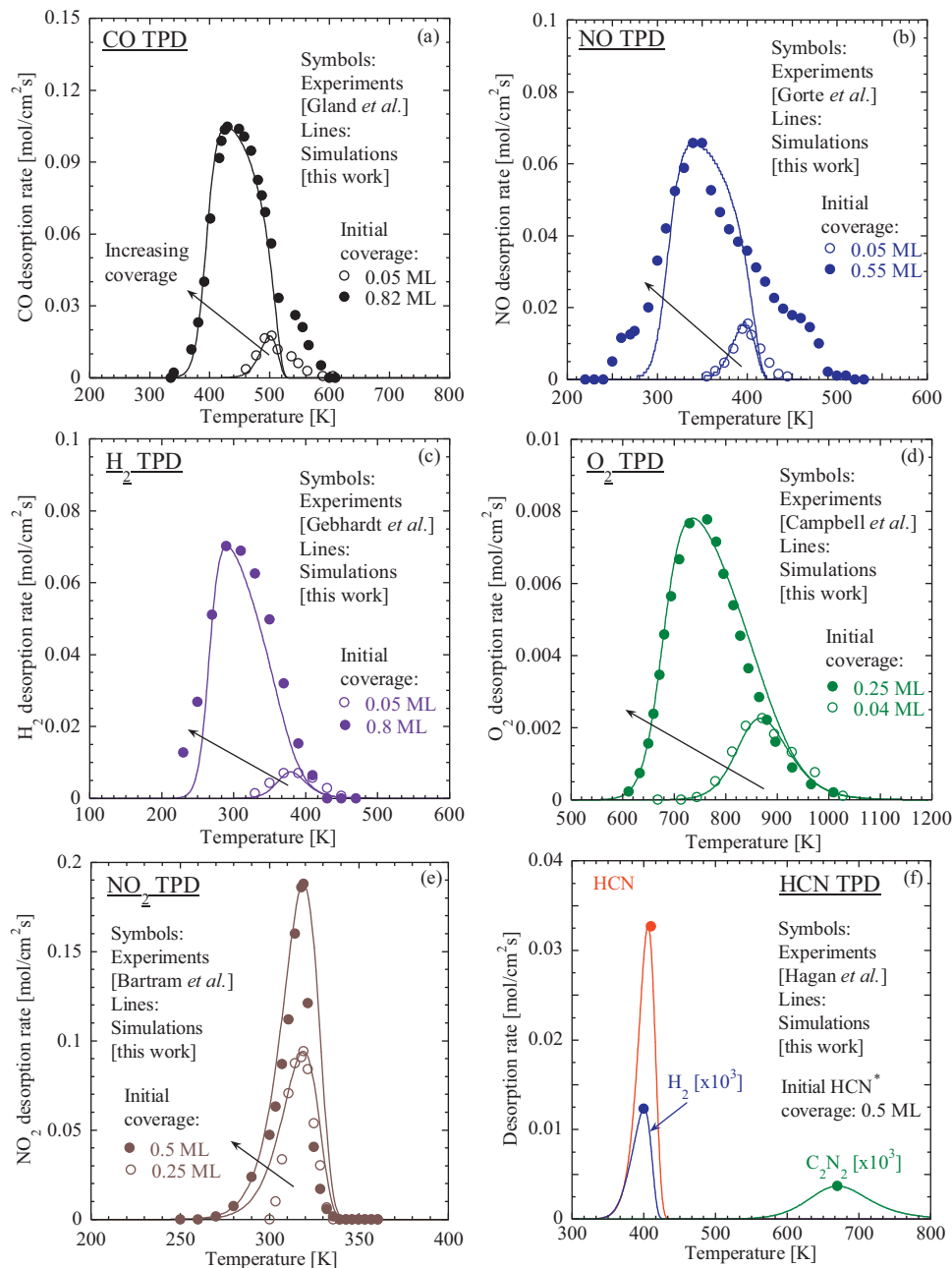


**Fig. 2.** UHV-TPD analysis of (a) CO, (b) NO, (c) H<sub>2</sub>, (d) O<sub>2</sub>, (e) NO<sub>2</sub>, and (f) HCN on Pt. Symbols represent the experimental data, whereas lines represent our simulations. Panel a: CO TPD [25]; initial high and low CO\* coverages are 0.82 ML and 0.05 ML, respectively; ramp rate = 13 K/s. Panel b: NO TPD [35]; initial high and low NO\* coverages are 0.55 ML and 0.05 ML, respectively; ramp rate = 10 K/s. Panel c: H<sub>2</sub> TPD [133]; initial high and low H\* coverages are 0.8 ML and 0.05 ML, respectively; ramp rate = 7.9 K/s. Panel d: O<sub>2</sub> TPD [116], initial high and low O<sup>\*</sup> coverages are 0.25 ML and 0.04 ML, respectively; ramp rate = 8 K/s. Panel e: NO<sub>2</sub> TPD [58]; initial high and low NO<sub>2</sub>\* coverages are 0.5 ML and 0.25 ML, respectively; ramp rate = 10 K/s. Panel f: HCN TPD [67]; initial HCN\* coverage is 0.5ML; ramp rate = 2 K/s. See Table 2 for the extracted kinetic parameters from these simulations.

CO<sub>2</sub>\* + \* ↔ CO\* + O\* is adjusted to 0.73 (starting from 0.5) to correctly capture the location of the CO<sub>2</sub> desorption peak. The bond index modification implemented here is similar to the earlier work (bond index = 0.8) by Mhadeshwar and Vlachos [29] for this reaction based on DFT-derived Polanyi-type relations in literature. The small difference originates from our use of TPR experimental data to extract the bond index. Fig. 3b shows the simulated coverage profiles. CO\* and O\* react on the surface at ~340 K to produce CO<sub>2</sub>\*, which desorbs. The excess CO\* desorbs at ~500 K. A small modification of CO binding energy to 40 kcal/mol ( $Q_{CO}^{avg}$  ~ 36 kcal/mol from TPD in Table 2), within the reported range in literature (29–54 kcal/mol), is carried out to correctly capture the experimental data. To validate the bond index modification, another set of TPR experimental

data for CO oxidation on Pt (initial coverages: 0.82 ML of CO\* and 0.17 ML of O\*) by Gland and Kollin [25] is also simulated without any parameter adjustment (Fig. 3c and d). The mechanism predictions are in excellent agreement with the experimental data. Overall, the reaction mechanism captures the CO oxidation chemistry well at UHV conditions.

### 3.2.2. NO oxidation

To extract some of the kinetic parameters for the NO oxidation chemistry, we have used the UHV-TPR experiments conducted on Pt(111) by Mudiyanselage et al. [73]. Initial coverages include 0.15 ML of NO\* and 0.75 ML of O\*. Bartram et al. [74] reported that NO oxidation to NO<sub>2</sub> is not favored on Pt(111) at low O\* coverage

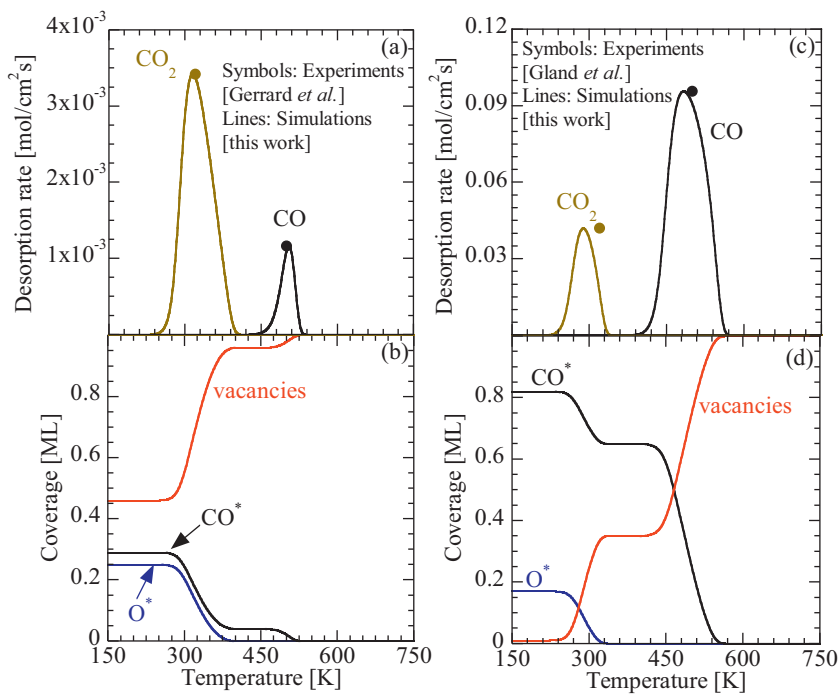


**Fig. 3.** Rate (panels a and c) and coverage (panels b and d) for UHV-TPR analysis of CO oxidation on Pt(111). Symbols represent the experimental data [25,26], whereas lines represent our simulations. Operating conditions for panels a and c: initial surface coverages O<sup>\*</sup> and CO<sup>\*</sup> are 0.25 ML and 0.29 ML, respectively; ramp rate = 1 K/s [26]. Operating conditions for panels b and d: initial surface coverages of O<sup>\*</sup> and CO<sup>\*</sup> are 0.17 ML and 0.82 ML, respectively; ramp rate = 13 K/s [25]. Simulations are in close agreement with the experimental data.

(~0.25 ML) due to the larger activation barrier for NO oxidation compared to NO desorption; however, they suggested the possibility of NO<sub>2</sub> formation at higher oxygen coverage (~0.75 ML). A DFT study of NO oxidation on Pt(111) by Ovesson et al. suggested that the oxidation is oxygen coverage ( $\theta_O$ ) dependent; and  $\theta_O$  needs to be more than 0.25 ML for the reaction to be favorable [62]. Along the similar lines, Mudiyanselage et al. reported NO oxidation to NO<sub>2</sub> with high  $\theta_O$  (~0.75 ML) on Pt(111) [73]. Without any adjustment of the kinetic parameters, we observe N<sub>2</sub> formation due to NO<sup>\*</sup> decomposition; however, N<sub>2</sub> formation was not reported in the TPR experiments. To slow down the NO<sup>\*</sup> decomposition chemistry, we have adjusted the bond index of the NO<sup>\*</sup> decomposition reaction pair R<sub>71</sub>–R<sub>72</sub>: NO<sup>\*</sup> + \* ⇌ N<sup>\*</sup> + O<sup>\*</sup> to 0.89 (starting from 0.5). This adjustment is consistent with the bond index modification reported earlier in Section 3.1.1 for decomposition reactions, where the increase in bond index typically results in increased activation energy. A minor adjustment of NO binding energy to 30.5 kcal/mol ( $Q_{NO}^{avg}$  ~29.2 kcal/mol from TPD in Table 2) is made to correctly capture the experimental data. As shown in Fig. 4a, the NO oxidation mechanism captures the experimental peaks for all three species (NO<sup>\*</sup>, NO<sub>2</sub><sup>\*</sup>, and O<sup>\*</sup>) very well.

Simulated coverage profiles, shown in Fig. 4b, indicate that NO<sup>\*</sup> oxidation starts immediately at low temperatures (>100 K) under the UHV conditions. This feature is also reported by Mieher et al. [75] in their NO oxidation experiments, where they observed exchange of oxygen between labeled NO and O<sub>2</sub>. Above ~200 K, we observe that NO<sub>2</sub><sup>\*</sup> decomposition to NO<sup>\*</sup> and O<sup>\*</sup> also becomes significant, therefore all of the NO<sup>\*</sup> is not oxidized to NO<sub>2</sub><sup>\*</sup>. At ~300 K, NO<sup>\*</sup> desorption results in the NO peak. At this temperature, most of the NO<sup>\*</sup> is re-generated from NO<sub>2</sub><sup>\*</sup> decomposition, which is also consistent with the increase in O<sup>\*</sup> coverage. Furthermore, NO<sub>2</sub> desorption also competes with NO<sub>2</sub><sup>\*</sup> decomposition, resulting in a smaller NO<sub>2</sub> desorption peak, consistent with the experimental observation by Mudiyanselage et al. [73]. Finally, the excess O<sup>\*</sup> desorbs at higher temperature (400–800 K), consistent with the

experiments. Overall, the surface reaction mechanism captures the NO oxidation chemistry very well as UHV conditions.

### 3.2.3. CH<sub>2</sub>O oxidation

UHV-TPR experimental data of Attard et al. [76] for CH<sub>2</sub>O oxidation on Pt(111) is used to simulate the CH<sub>2</sub>O oxidation chemistry. Here, the initial coverages include 0.5 ML of CH<sub>2</sub>O<sup>\*</sup> and 0.3 ML of O<sup>\*</sup>. As shown in Fig. 5a, the simulated peak temperatures of the gaseous products are in close agreement with the reported experimental data, without any modification of the initial kinetic parameters. We note that the model predicted peak for CH<sub>2</sub>O desorption (198 K) is higher than the experimentally reported value (134 K); however the model predicted peak and the corresponding binding energy of CH<sub>2</sub>O (see Table 2) are consistent with other CH<sub>2</sub>O TPD experiments [64,77] (see Section 3.1) as well as literature DFT estimates [65,66].

Simulated coverage profiles, shown in Fig. 5b, indicate that at ~150 K, CH<sub>2</sub>O<sup>\*</sup> and O<sup>\*</sup> coverages start to decrease, resulting in the formation of CO<sup>\*</sup>, H<sup>\*</sup>, and OH<sup>\*</sup>. RPA shows that reaction R<sub>99</sub>: CH<sub>2</sub>O<sup>\*</sup> + \* → HCO<sup>\*</sup> + H<sup>\*</sup> is dominant in this region. Once formyl (HCO<sup>\*</sup>) is produced, it rapidly oxidizes to CO<sup>\*</sup> and OH<sup>\*</sup> through reaction R<sub>108</sub>: HCO<sup>\*</sup> + O<sup>\*</sup> → CO<sup>\*</sup> + OH<sup>\*</sup>. With further increase in the temperature, formyl oxidizes to H<sub>2</sub>O<sup>\*</sup> through reaction R<sub>110</sub>: HCO<sup>\*</sup> + OH<sup>\*</sup> → H<sub>2</sub>O<sup>\*</sup> + CO<sup>\*</sup>, which subsequently results in H<sub>2</sub>O desorption at ~200 K. This is also consistent with the decrease in OH<sup>\*</sup> coverage at this temperature. The second water peak at ~250 K (much smaller and not observed experimentally) is due to the reaction between OH<sup>\*</sup> and H<sup>\*</sup>. The model predictions also show a very small CO<sub>2</sub> desorption peak at ~260 K (magnified by a factor of 10,000), consistent with the experiments. This peak is due to reaction R<sub>28</sub>: CO<sup>\*</sup> + OH<sup>\*</sup> → CO<sub>2</sub><sup>\*</sup> + H<sup>\*</sup>. With further increase in the temperature, H<sup>\*</sup> (primarily formed from CH<sub>2</sub>O<sup>\*</sup> decomposition) associatively desorbs (R<sub>14</sub>: 2H<sup>\*</sup> → H<sub>2</sub> + 2\*) at ~280 K, similar to the experimentally observed peak. Finally, the only species left on the surface is CO<sup>\*</sup>, which desorbs at ~495 K, consistent with the

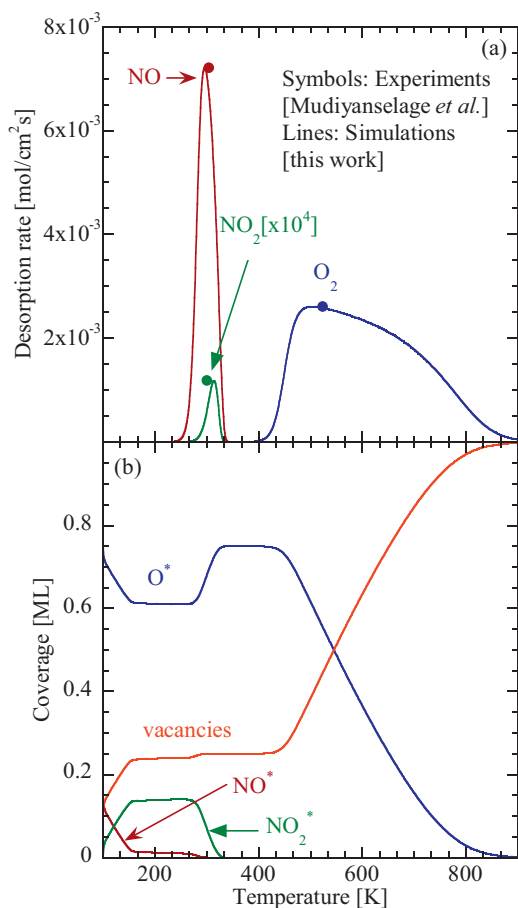


**Fig. 4.** Rate (panel a) and coverage (panel b) profiles for UHV-TPR analysis of NO oxidation on Pt(111). Symbols represent the experimental data [73], whereas lines represent our simulations. Operating conditions: initial surface coverages of O\* and NO\* are 0.75 ML and 0.15 ML, respectively; ramp rate = 2 K/s. Simulations are in close agreement with the experimental data.

experiments. Overall, the CH<sub>2</sub>O oxidation mechanism shows excellent agreement with the experimentally observed peaks for multiple products under the UHV conditions, without any adjustment of the kinetic parameters.

### 3.2.4. NH<sub>3</sub> oxidation

Some of the kinetic parameters for NH<sub>3</sub> oxidation are extracted from the UHV-TPR experimental data on Pt(111) reported by Mieher and Ho [78]. Initial coverages include 0.12 ML of NH<sub>3</sub>\* and 0.25 ML of O\*. The mechanism predictions for rates and coverages are shown in Fig. 6a and b, respectively. Even though there is some discrepancy in the H<sub>2</sub>O desorption peak (238 K vs. 350 K), we have verified the H<sub>2</sub>O binding energy from additional TPD experiments [79,80] (see Section 3.1) and literature DFT calculations [81,82]. The mechanism predictions for other gaseous products (NO and N<sub>2</sub>) are in excellent agreement with the experimental data. Increasing the NH<sub>3</sub> binding energy from 20.7 kcal/mol to ~33.5 kcal/mol helps in capturing the H<sub>2</sub>O desorption peak at 350 K (as it delays reaction R<sub>62</sub>: NH<sub>3</sub>\* + OH\* → NH<sub>2</sub>\* + H<sub>2</sub>O\*), but such modification is beyond the accepted literature range reported in Table 2; hence, it is not carried out. Decreasing the binding energy of NH<sub>2</sub> to 39–47 kcal/mol [53,83–85], which has been reported in literature using UBI-QEP and DFT calculations for less stable configurations (top sites), has a similar effect of shifting the water peak to higher temperature. However, such modification is also inconsistent with the literature binding energy values for stable configurations (bridge sites)

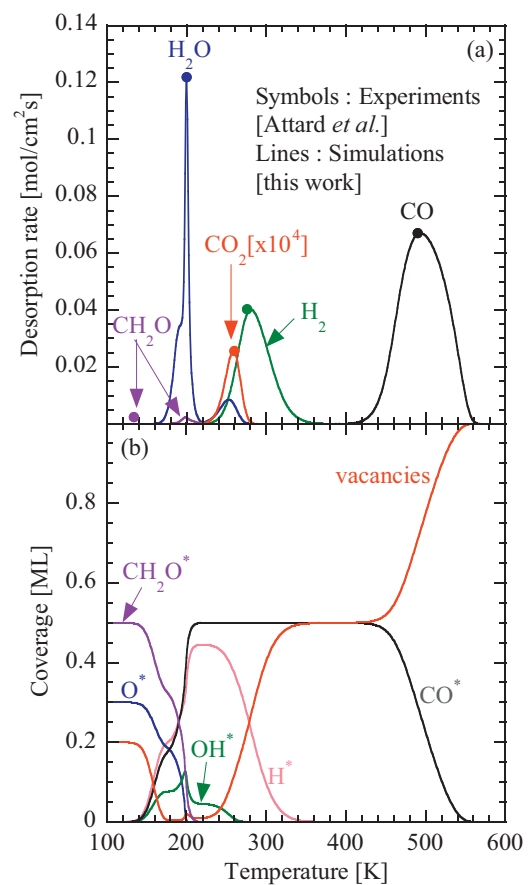


**Fig. 5.** Rate (panel a) and coverage (panel b) profiles for UHV-TPR analysis of CH<sub>2</sub>O oxidation on Pt(110). Symbols represent the experimental data [76], whereas lines represent our simulations. Operating conditions: initial surface coverages of O\* and CH<sub>2</sub>O\* are 0.3 ML and 0.5 ML, respectively; ramp rate = 10 K/s. Simulations are in good agreement with the experimental data.

using DFT calculations (54–58 kcal/mol [53,55,83,85]) (see Table 2); hence, it is not carried out.

Simulated coverage profiles in Fig. 6b provide some insights about the surface chemistry, but RPA is required to understand the dominant reactions in the NH<sub>3</sub> oxidation chemistry. RPA at 150 K shows that NH<sub>3</sub>\* undergoes oxidative dehydrogenation through reaction R<sub>55</sub>: NH<sub>3</sub>\* + O\* → NH<sub>2</sub>\* + OH\*. As soon as OH\* is formed, both OH\* and O\* participate in the oxidative dehydrogenation reactions R<sub>62</sub>: NH<sub>3</sub>\* + OH\* → NH<sub>2</sub>\* + H<sub>2</sub>O\* and R<sub>58</sub>: NH<sub>2</sub>\* + O\* → NH\* + OH\*, resulting in the formation of NH\*. Water formed in reaction R<sub>62</sub> desorbs, which is also observed in the experiments. RPA at 400 K and 450 K shows that there are four competing pathways for NH\* consumption, viz., reaction R<sub>76</sub>: NH\* + O\* → NO\* + H\* that subsequently results in the NO desorption peak, as well as reactions R<sub>60</sub>: NH\* + O\* → N\* + OH\*, R<sub>53</sub>: NH\* + \* → N\* + H\*, and R<sub>66</sub>: NH\* + OH\* → N\* + H<sub>2</sub>O\* that eventually lead to the N<sub>2</sub> desorption peak. The second water peak (much smaller and not observed experimentally) at higher temperature (~450 K) is due to reactions R<sub>22</sub>: OH\* + H\* → H<sub>2</sub>O\* + \* and R<sub>24</sub>: 2OH\* → H<sub>2</sub>O\* + O\*. We have adjusted the bond indices of reaction pairs R<sub>75</sub>–R<sub>76</sub>, R<sub>53</sub>–R<sub>54</sub>, R<sub>59</sub>–R<sub>60</sub>, and R<sub>65</sub>–R<sub>66</sub> to 0.23, 0.57, 0.65, and 0.71 (starting from 0.5), respectively, to improve the agreement with experimental data. The bond index modification, although brute-force, is necessary to ensure that both NO and N<sub>2</sub> peaks are observed in the simulations and to capture the correct kinetics for the formation of multiple products. Finally, excess oxygen, albeit negligible (~0.02 ML), desorbs at higher temperatures (~820 K).

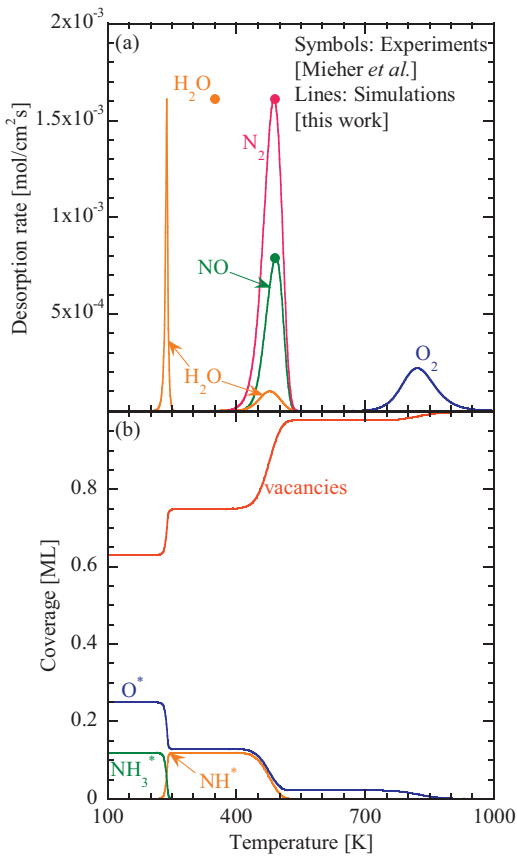


**Fig. 6.** Rate (panel a) and coverage (panel b) profiles for UHV-TPR analysis of NH<sub>3</sub> oxidation on Pt(111). Symbols represent the experimental data [78], whereas lines represent our simulations. Operating conditions: initial surface coverages of O<sup>\*</sup> and NH<sub>3</sub><sup>\*</sup> are 0.25 ML and 0.12 ML, respectively; ramp rate = 2 K/s. Simulations are in good agreement with the experimental data. Discrepancy in the peak locations for H<sub>2</sub>O and O<sub>2</sub> is discussed in the text.

The O<sub>2</sub> peak was not reported by Mieher and Ho [78], as the experiments were carried out only up to 700 K.

### 3.2.5. HCN oxidation

UHV-TPR simulations for HCN oxidation are compared against the experimental data on Pt(112) reported by Guo et al. [86]. Here, the initial coverages include 0.67 ML of HCN<sup>\*</sup> and 0.25 ML of O<sup>\*</sup>. Simulated rate and coverage profiles are shown in Fig. 7a and b, respectively. A number of products are observed in the TPR experiment, viz., unreacted HCN, CO, CO<sub>2</sub>, H<sub>2</sub>O, H<sub>2</sub>, N<sub>2</sub>, and C<sub>2</sub>N<sub>2</sub>. We have modified the bond index of the reaction pair R<sub>87</sub>–R<sub>88</sub>: HCN<sup>\*</sup> + O<sup>\*</sup> ⇌ CN<sup>\*</sup> + OH<sup>\*</sup> to 0.44 (starting from 0.5) to correctly capture most of the product peak temperatures.

RPA at low temperature shows that HCN<sup>\*</sup> oxidizes to CN<sup>\*</sup> via reaction R<sub>87</sub>: HCN<sup>\*</sup> + O<sup>\*</sup> → CN<sup>\*</sup> + OH<sup>\*</sup>. As soon as OH<sup>\*</sup> is formed, it oxidizes HCN<sup>\*</sup> to CN<sup>\*</sup> and H<sub>2</sub>O<sup>\*</sup> via reaction R<sub>89</sub>: HCN<sup>\*</sup> + OH<sup>\*</sup> → CN<sup>\*</sup> + H<sub>2</sub>O<sup>\*</sup>. Water desorbs immediately after the formation at ~260 K, consistent with the experiments. At the same temperature, CN<sup>\*</sup> is oxidized to produce CO<sup>\*</sup> and N<sup>\*</sup> via reaction R<sub>94</sub>: CN<sup>\*</sup> + O<sup>\*</sup> → CO<sup>\*</sup> + N<sup>\*</sup>. CO<sup>\*</sup> reacts with O<sup>\*</sup> to form CO<sub>2</sub><sup>\*</sup> via reaction R<sub>10</sub>: CO<sup>\*</sup> + O<sup>\*</sup> → CO<sub>2</sub><sup>\*</sup> + \*, which desorbs at ~260 K, whereas N<sub>2</sub> desorbs at ~280 K. We note that our model predictions show CO<sub>2</sub> and N<sub>2</sub> formation at significantly lower temperatures than those reported in the experiments. In case of CO<sub>2</sub>, we have rigorously validated the CO oxidation activation energy (and temperature) from other TPR experiments reported in Sections 3.2.1 and 3.2.3. The discrepancy in N<sub>2</sub> formation peak could be due to potentially missing reaction pathways in our reaction network. However,

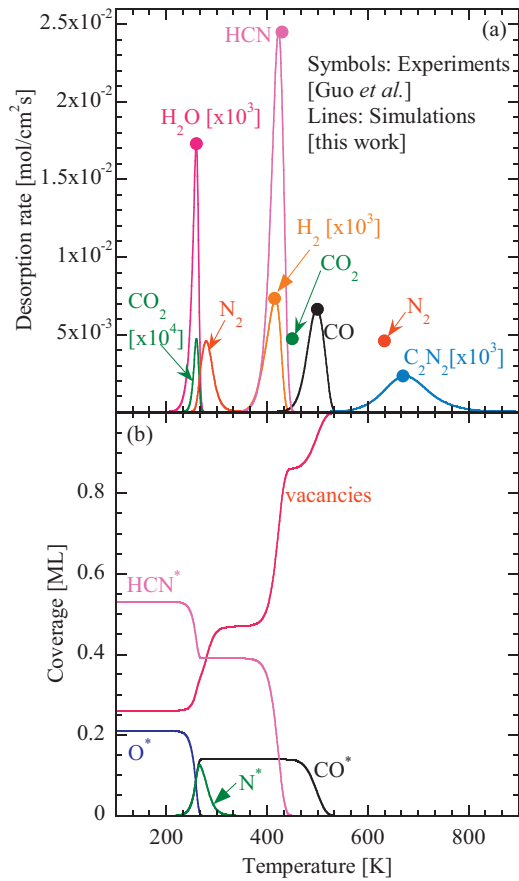


**Fig. 7.** Rate (panel a) and coverage (panel b) profiles for UHV-TPR analysis of HCN oxidation on Pt(112). Symbols represent the experimental data [86], whereas lines represent our simulations. Operating conditions: initial surface coverages of O<sup>\*</sup> and HCN<sup>\*</sup> are 0.25 ML and 0.67 ML, respectively; ramp rate = 2 K/s. Simulations are in reasonable agreement with the experimental data. Discrepancy in the peak locations for CO<sub>2</sub> and N<sub>2</sub> is discussed in the text.

under the practical operating conditions of emissions *oxidation* to partially and fully oxidized products, the formation of N<sub>2</sub> (a *reduction* product) is less important for a DOC. Nonetheless, it is certainly a limitation of the proposed surface reaction mechanism. The model correctly captures the H<sub>2</sub> desorption peak at ~415 K, which originates from the decomposition reaction R<sub>85</sub>: HCN<sup>\*</sup> + \* → H<sup>\*</sup> + CN<sup>\*</sup>. The unreacted HCN desorbs at ~425 K and the remaining CO<sup>\*</sup> desorbs at ~500 K, consistent with the experiments. Finally, a small quantity of cyanogen (C<sub>2</sub>N<sub>2</sub><sup>\*</sup>), formed from reaction R<sub>124</sub>: 2CN<sup>\*</sup> → C<sub>2</sub>N<sub>2</sub><sup>\*</sup> + \* desorbs at a much higher temperature (~675 K), consistent with the experiments. As seen from this analysis, HCN oxidation is a very complicated chemistry, and it is quite challenging to capture the formation of all the products. Our surface reaction mechanism shows the formation of all important products observed in the UHV conditions, and captures most of the product desorption peak locations.

## 4. Mechanism performance and validation under practically more relevant operating conditions

Most of the kinetic parameters in our emissions oxidation surface reaction mechanism are extracted from UHV-TPD/TPR experiments on single crystal surfaces, but it is also important to assess the mechanism performance at practically relevant operating conditions. Such conditions include monolith and fixed bed experiments conducted at atmospheric pressure with dilute levels of emissions in the feed at short residence times. As the typical

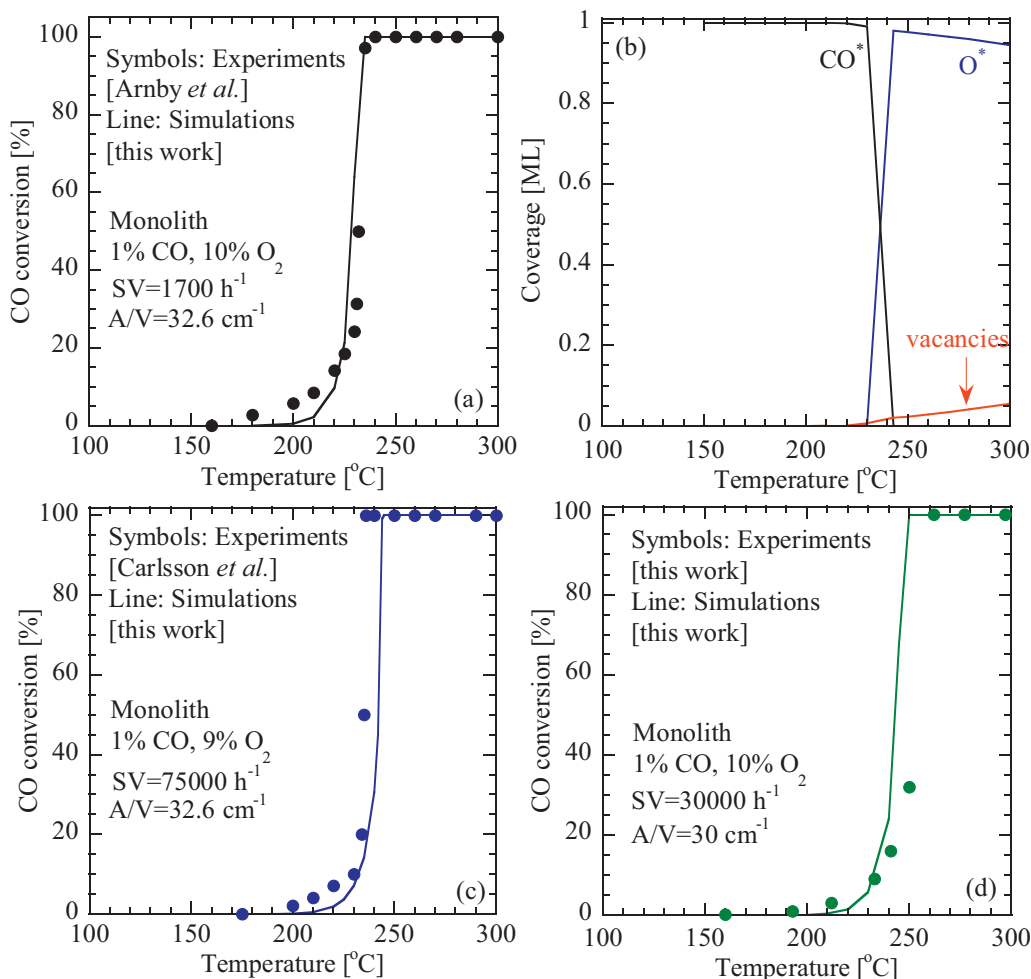


**Fig. 8.** Performance (panel a), analysis (panel b), and validation (panels c and d) of the microkinetic model for CO oxidation on Pt monoliths. Symbols represent the experimental data, whereas lines represent our simulations. Operating conditions for panels a and b: Pt/Al<sub>2</sub>O<sub>3</sub> monolith [87]; feed of 1% CO, 10% O<sub>2</sub>, and 89% Ar; space velocity of 17,000 h<sup>-1</sup>; and catalyst area per unit reactor volume of 32.6 cm<sup>-1</sup>. Operating conditions for panel c: Pt/Al<sub>2</sub>O<sub>3</sub> monolith [91]; feed of 1% CO, 9% O<sub>2</sub>, and 90% N<sub>2</sub>; space velocity of 75,000 h<sup>-1</sup>; and catalyst area per unit reactor volume of 32.6 cm<sup>-1</sup>. Operating conditions for panel d: Pt/ZnO monolith (this work); feed of 1% CO, 10% O<sub>2</sub>, 9% N<sub>2</sub>, and 80% Ar; space velocity of 30,000 h<sup>-1</sup>, and catalyst area per unit reactor volume of 30 cm<sup>-1</sup>. A Dycor Dymaxion mass spectrometer and Agilent Micro GC 3000A were used for identification and quantification of the gaseous species in the product stream. Simulations are in close agreement with the experimental data.

concentration levels of emissions considered in this paper are very low (few tens to hundreds of ppm), we have selected relevant literature experiments consistent with such levels. To simulate the steady state experimental data, here we use an isothermal plug flow reactor (PFR) model. The assumption about isothermality is based on the very small amount of heat generated during the oxidation of dilute concentration levels for the emissions components (except for 1% CO, but here the experimental data is reported at controlled steady state temperatures). Finally, it is important to note that the kinetic parameters extracted from UHV conditions on single crystal surfaces provide an excellent estimate for the simulations discussed in this section. However, some minor parameter tuning is expected given the pressure (UHV vs. atmospheric) and materials (single crystals vs. polycrystalline and supported catalysts) gap.

#### 4.1. CO oxidation

Simulations using our CO oxidation reaction mechanism from Appendix A (Table S1) are compared against three sets of experiments conducted with monolith catalysts. The first comparison, shown in Fig. 8a, is against the experiments conducted with a Pt/γ-Al<sub>2</sub>O<sub>3</sub> monolith [87]. The support and catalyst details

are as follows [87]: monolith length = 2.3 cm, monolith diameter = 1.3 cm, monolith cell density = 400 cells per square inch (CPSI), washcoat loading = 0.15 g, Pt content = 0.3 mg, and BET surface area = 151 m<sup>2</sup>/g of washcoat.

Only two kinetic parameters (pre-exponential factor for reactions R<sub>10</sub>: CO\* desorption and R<sub>10</sub>: CO\* oxidation) were slightly modified to  $5.7 \times 10^{16}$  s<sup>-1</sup> (starting from  $1 \times 10^{16}$  s<sup>-1</sup> [88]) and  $1 \times 10^{10}$  s<sup>-1</sup> (starting from  $1 \times 10^{11}$  s<sup>-1</sup>), respectively, to capture the experimental data. Surface coverages in Fig. 8b show that the surface is poisoned by CO\* at low temperatures, consistent with the previous literature studies [27,89,90]. With increase in temperature, CO\* starts to desorb, freeing up the vacancies for O<sub>2</sub> dissociative adsorption and subsequent CO\* oxidation. At higher temperatures, as CO\* is completely consumed, O\* is the most abundant reaction intermediate (MARI) on the catalyst surface. We note that the pre-exponential factors proposed here for CO oxidation are different (approximately by an order of magnitude) from the ones reported by Mhadeshwar and Vlachos [29], but such discrepancy is expected given the different types of experimental data selected (ignition and molecular beam data in the earlier paper vs. monolith and fixed bed data in this work).

We also validated the CO oxidation mechanism against experimental data on a Pt/Al<sub>2</sub>O<sub>3</sub> monolith reported by Carlsson and

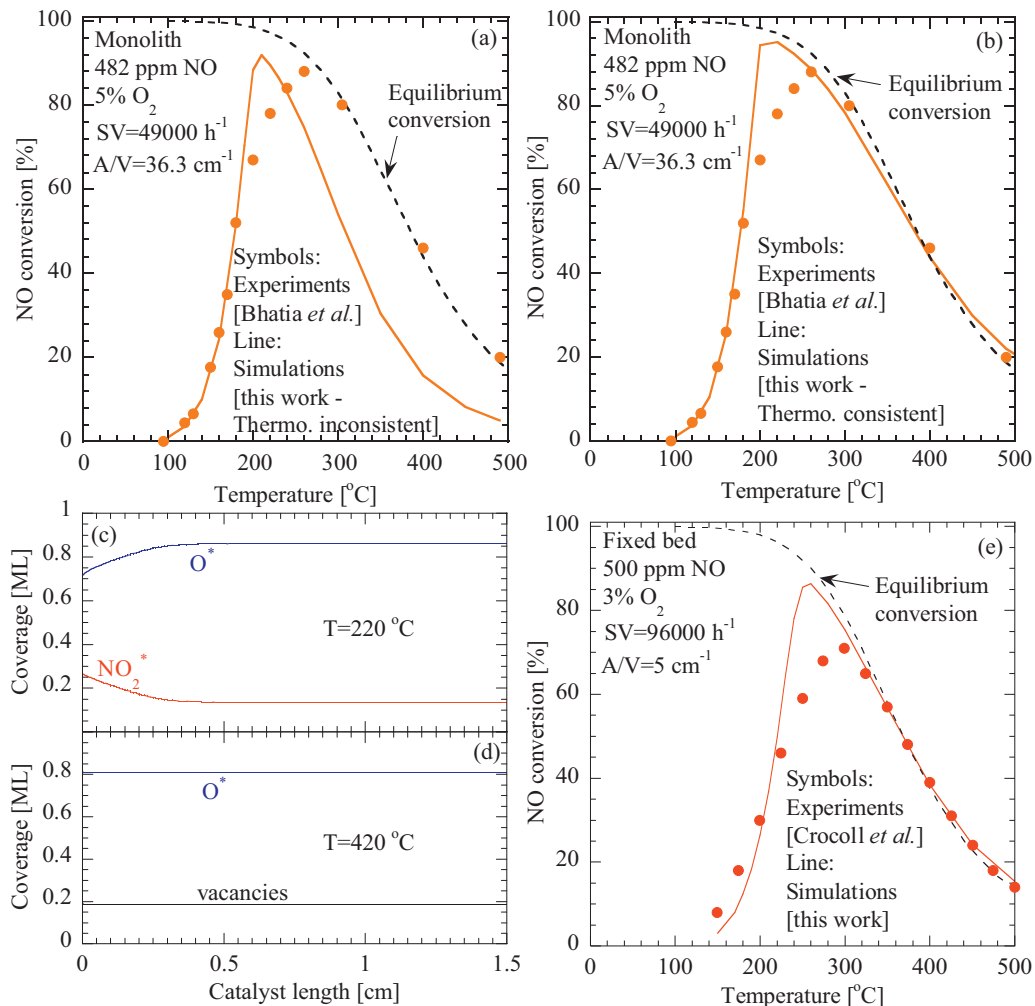


**Fig. 9.** Performance (panel a and b), analysis (panels c and d), and validation (panel e) of the microkinetic model for NO oxidation on Pt monolith and fixed bed. Symbols represent the experimental data; solid lines represent our simulations; and dashed lines represent the equilibrium calculations using GASEQ software [94]. Panel b shows the improvement in mechanism predictions after ensuring thermodynamic consistency (see text for details). Operating conditions for panels a-d: Pt/Al<sub>2</sub>O<sub>3</sub> monolith [93]; feed of 482 ppm NO, 5% O<sub>2</sub>, and ~95% N<sub>2</sub>; space velocity of 49,000 h<sup>-1</sup>; and catalyst area per unit reactor volume of 36.3 cm<sup>-1</sup>. Operating conditions for panel e: Pt/Al<sub>2</sub>O<sub>3</sub> fixed bed [32]; feed of 500 ppm NO, 3% O<sub>2</sub>, and ~97% N<sub>2</sub>, space velocity 96,000 h<sup>-1</sup>, and catalyst area per unit reactor volume of 5 cm<sup>-1</sup>. Simulations are in close agreement with the experimental data.

Skoglundh [91] as well as against our BenchCAT [92] experiments on a Pt/ZnO monolith. In the experiments conducted by Carlsson and Skoglundh [91], support and catalyst details are as follows: monolith length = 1.5 cm, monolith diameter = 1.2 cm, monolith cell density = 400 CPSI, washcoat loading = 0.2 g, and catalyst coating = 0.12 g/cm<sup>3</sup>. On the other hand, support and catalyst details for the experiments carried out in our lab are as follows: monolith length = 1 cm, channel size = 1 mm × 1 mm, total channels = 6, BET surface area = 6.4 m<sup>2</sup>/g, Pt particle diameter = 2.6 nm, Pt loading = 2%, and monolith cell density = 400 CPSI. The mechanism predictions, without any parameter modification, are shown in Fig. 8c and d, for the respective experiments. Overall, the proposed reaction mechanism captures the CO oxidation chemistry well against multiple experimental data sets at practically relevant operating conditions.

#### 4.2. NO oxidation

Fig. 9 shows the comparison of our model predictions with monolith and fixed bed reactor experiments for NO oxidation on Pt [32,93]. The literature experiments reported by Bhatia et al. [93] were carried out using practically relevant NO and O<sub>2</sub> concentration

levels (482 ppm and 5%, respectively) on a Pt/Al<sub>2</sub>O<sub>3</sub> coated monolith (Fig. 9a and b). Similarly, fixed bed reactor experiments were carried out by Crocoll et al. [32] using 500 ppm of NO and 3% O<sub>2</sub> (Fig. 9e). Support and catalyst details for the experiments by Bhatia et al. [93] are as follows: monolith length = 1.5 cm, monolith diameter = 1.7 cm, monolith cell density = 400 CPSI, Pt loading = 70 g/ft<sup>3</sup>, Pt loading = 2.63 wt %, Pt dispersion = 20.3%, Pt area = 2.21 m<sup>2</sup>/g of washcoat, and Pt particle size = 5.59 nm. Similarly, the support and catalyst details for the NO oxidation experiment by Crocoll et al. [32] are as follows: Pt/γ-Al<sub>2</sub>O<sub>3</sub> powder catalyst, Pt loading = 2%, BET surface area = 175 m<sup>2</sup>/g, total pore volume = 0.70 cm<sup>3</sup>/g, pore diameter = 8.6 nm, active Pt surface area = 5.3 m<sup>2</sup>/g<sub>(Pt)</sub>, and catalyst weight = 1 g.

Unlike CO oxidation, the experimental data show that NO conversion decreases after ~250 °C. Equilibrium calculations conducted using GASEQ software [94] at the high temperature conditions indicate that the experimental data for NO oxidation are equilibrium limited. RPA indicates that the oxidation of NO\* via R<sub>80</sub>: NO\* + O\* → NO<sub>2</sub>\* + \* is the most important step in the kinetically controlled low temperature region; and its pre-exponential factor was slightly tuned from  $1 \times 10^{11}$  s<sup>-1</sup> to  $3 \times 10^{12}$  s<sup>-1</sup> to improve the agreement with the experimental data. Minor adjustment of

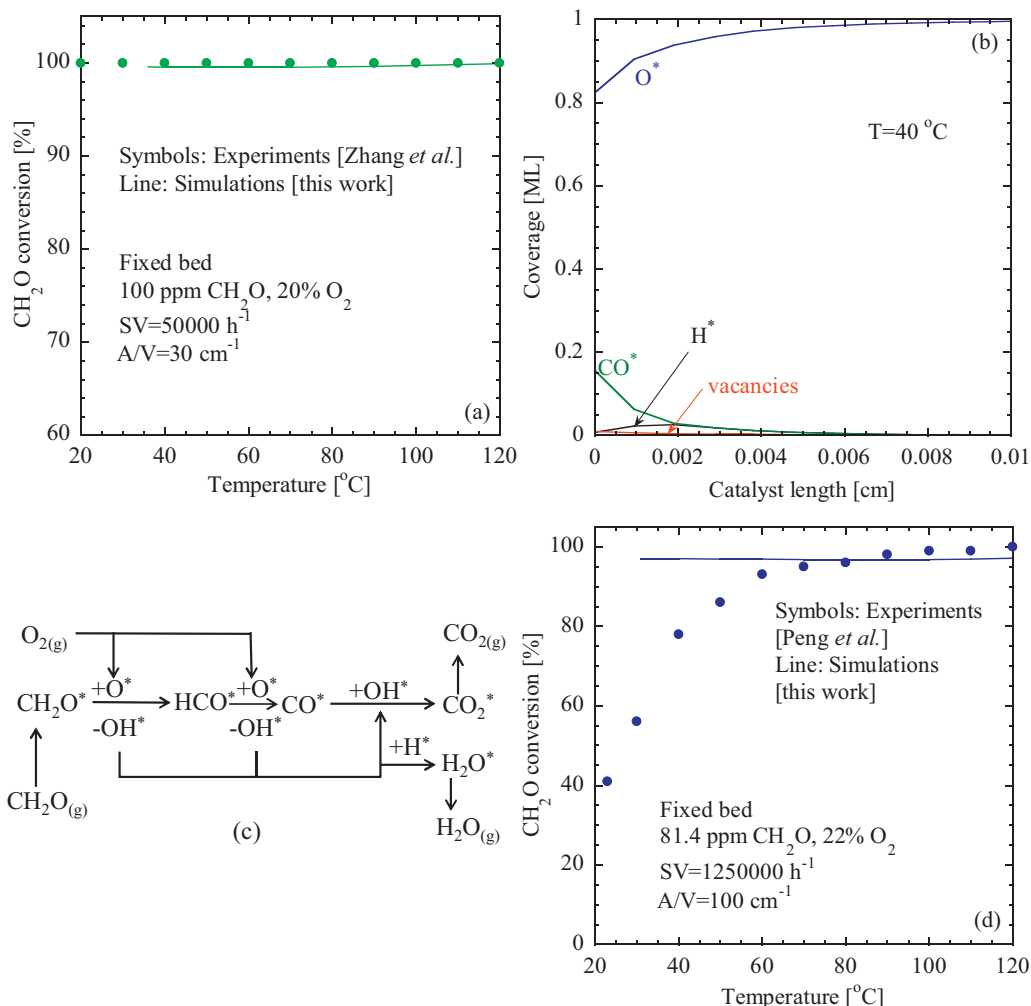


**Fig. 10.** Performance (panel a), analysis (panels b and c), and validation (panel d) of the microkinetic model for  $\text{CH}_2\text{O}$  oxidation on Pt fixed beds. Symbols represent the experimental data, whereas lines represent our simulations. Panel b shows the coverage profiles of dominant surface species along the catalyst length (actual length = 0.47 cm) at  $40^{\circ}\text{C}$ . Panel c shows the dominant reaction pathways in the  $\text{CH}_2\text{O}$  oxidation chemistry at  $40^{\circ}\text{C}$  (at the entrance of the catalyst). Operating conditions for panels a–c: Pt/TiO<sub>2</sub> fixed bed [98]; feed of 100 ppm  $\text{CH}_2\text{O}$ , 20%  $\text{O}_2$ , and ~80% He; space velocity of 50,000  $\text{h}^{-1}$ ; and catalyst area per unit reactor volume of 30  $\text{cm}^{-1}$ . Operating conditions for panel d: Pt/TiO<sub>2</sub> fixed bed [99]; feed of 81.4 ppm  $\text{CH}_2\text{O}$ , 22%  $\text{O}_2$ , and ~78%  $\text{N}_2$ ; space velocity of 1,250,000  $\text{h}^{-1}$ ; and catalyst area per unit reactor volume of 100  $\text{cm}^{-1}$ . Simulations are in reasonable agreement with the experimental data. Discrepancy in panel d due to high space velocity is discussed in the text.

$\text{NO}_2$  binding energy to 23.5 kcal/mol ( $Q_{\text{NO}_2}^{\text{TPD}} = 19$  kcal/mol, literature range 17–38 kcal/mol [48,57,59,61–63,74]) is also carried out to improve the low temperature (kinetically controlled region) NO conversion predictions. Despite such modifications, the model predictions severely under predict the higher temperature equilibrium limited data in Fig. 9a.

The origin of this discrepancy at high temperature is associated with the lack of thermodynamic (primarily entropic) consistency of kinetic parameters, as discussed by several previous papers [30,93,95–97]. Maintaining thermodynamic consistency is critical, especially for correctly capturing the equilibrium limited data. In our reaction mechanism, this is accomplished by a modified Arrhenius equation with temperature exponent  $\beta$  of  $-0.93$  (forward) and  $+0.93$  (backward) for reaction pair R<sub>79</sub>–R<sub>80</sub>:  $\text{NO}_2^* + * \leftrightarrow \text{NO}^* + \text{O}^*$ , (where  $k = A(T/T_0)^{\beta} e^{-E/RT}$  and  $T_0$  is 300 K). This allows one to match the entropy values for gas phase NO oxidation to  $\text{NO}_2$  ( $\text{NO} + \text{O} \rightarrow \text{NO}_2$ ) with the overall catalytic pathway for NO oxidation to  $\text{NO}_2$  (NO adsorption, oxygen adsorption,  $\text{NO}^* + \text{O}^* \rightarrow \text{NO}_2^* + *$ , and  $\text{NO}_2$  desorption). Including temperature exponents through a modified Arrhenius equation is a standard practice in gas phase reaction mechanism development community [41]; and it is also consistent

with the approach for catalytic reaction mechanisms to fulfill the thermodynamic constraints determined by Hess's law, as described by Mhadeshwar et al. [96]. Performance of the thermodynamically consistent NO oxidation reaction mechanism is shown in Fig. 9b. The agreement with experimental data is significantly improved under the equilibrium limited high temperature conditions.

Simulated coverage profiles along the catalyst length at two different temperatures ( $240^{\circ}\text{C}$  and  $420^{\circ}\text{C}$  corresponding to kinetically controlled and equilibrium limited regions, respectively) are shown in Fig. 9c and d. Under both conditions, the catalyst surface is predominantly covered by  $\text{O}^*$ , which is consistent with the high  $\text{O}_2$  concentration in the feed compared to that of NO.  $\text{NO}_2^*$  coverage is non-negligible in the kinetically controlled region due to  $\text{NO}^*$  oxidation, but it is negligible in the equilibrium limited region due to  $\text{NO}_2^*$  desorption.

The thermodynamically consistent NO oxidation mechanism is further validated against fixed bed experimental data of Crocoll et al. [32] without any further modification of the kinetic parameters. As shown in Fig. 9e, the NO oxidation mechanism predicts the conversion profile well in both kinetically controlled and equilibrium limited regions.

### 4.3. $\text{CH}_2\text{O}$ oxidation

The  $\text{CH}_2\text{O}$  oxidation reaction mechanism is compared against two sets of experimental data [98,99], as shown in Fig. 10a and d. Some of the operating conditions in the first set of experiments ( $\text{CH}_2\text{O}$  concentration of 100 ppm, space velocity of  $50000 \text{ h}^{-1}$ ) on Pt/TiO<sub>2</sub> fixed bed are reasonably close to the typical conditions in diesel engine exhaust aftertreatment; however, the O<sub>2</sub> level is much higher (20%). In the second set of experiments, the space velocity is so high ( $1,250,000 \text{ h}^{-1}$ ) that it does not represent practically relevant operating conditions (extremely short catalyst length). Under such conditions, we believe that mass transfer limitations will dominate over the surface kinetics, but we have still included this data set as a validation of our mechanism under extreme conditions. Support and catalyst details for the experiments by Zhang et al. [98] are as follows: Pt/TiO<sub>2</sub> powder catalyst, Pt loading = 1 wt.%, Pt particle size = ~1 nm, and BET surface area =  $47.4 \text{ m}^2/\text{g}$ . Similarly, the support and catalyst details for the experiments by Peng and Wang [99] are as follows: Pt/TiO<sub>2</sub> powder catalyst, BET surface area =  $61.5 \text{ m}^2/\text{g}$ , pore volume =  $0.24 \text{ cm}^3/\text{g}$ , average pore diameter = 11.5 nm, support particle size = 15.4 nm, Pt dispersion = 68.5%, Pt metal size = 1.5 nm, and catalyst weight = 0.25 g.

In the first set of experiments (Fig. 10a), it is observed that  $\text{CH}_2\text{O}$  oxidation is close to 100% even at room temperature. The surface coverage profiles along the catalyst length at  $40^\circ\text{C}$  (Fig. 10b) show that O<sup>\*</sup> is the MARI, whereas CO<sup>\*</sup> (produced from  $\text{CH}_2\text{O}^*$ ) is rapidly consumed at the catalyst entrance. Decrease in CO<sup>\*</sup> coverage is consistent with increase in H<sup>\*</sup> coverage due to reaction R<sub>28</sub>:  $\text{CO}^* + \text{OH}^* \rightarrow \text{CO}_2^* + \text{H}^*$ . RPA in Fig. 10c shows that  $\text{CH}_2\text{O}^*$  oxidation leads to the formation of formyl, which is further oxidized to CO<sup>\*</sup> and OH<sup>\*</sup> via reaction R<sub>108</sub>:  $\text{HCO}^* + \text{O}^* \rightarrow \text{CO}^* + \text{OH}^*$ . The intermediates CO<sup>\*</sup> and OH<sup>\*</sup> react via reaction R<sub>28</sub> to produce CO<sub>2</sub><sup>\*</sup> and H<sup>\*</sup>. Finally, H<sup>\*</sup> is completely oxidized to H<sub>2</sub>O<sup>\*</sup> via reaction R<sub>22</sub>:  $\text{H}^* + \text{OH}^* \rightarrow \text{H}_2\text{O}^* + *$ . This is consistent with the  $\text{CH}_2\text{O}$  oxidation experiments of McCabe and McCready [100], who suggested that CO and H are reaction intermediates that subsequently oxidize to form CO<sub>2</sub> and H<sub>2</sub>O. Based on the RPA, we have modified only one pre-exponential factor for the most important reaction R<sub>108</sub> from  $1 \times 10^{11} \text{ s}^{-1}$  to  $1.5 \times 10^{12} \text{ s}^{-1}$  to improve the agreement with the experiments. For the second set of experiments, despite the severe mass transfer limitations, our  $\text{CH}_2\text{O}$  oxidation mechanism reasonably predicts the experimental data at temperatures higher than  $60^\circ\text{C}$  without any further parameter modification. The evaluation of mass transfer limitations in this specific experiment is beyond the scope of the current work.

### 4.4. NH<sub>3</sub> oxidation

Fig. 11a compares the performance of our NH<sub>3</sub> oxidation reaction mechanism against the fixed bed reactor experiments on Pt/Al<sub>2</sub>O<sub>3</sub> [101]. The support and catalyst details are as follows [101]: Pt/Al<sub>2</sub>O<sub>3</sub> powder catalyst, BET surface area =  $120 \text{ m}^2/\text{g}$ , catalyst pore volume =  $0.81 \text{ cm}^3/\text{g}$ , Pt loading = 2%, and catalyst weight = 0.3 g. Here, 700 ppm of NH<sub>3</sub> was oxidized using 8% O<sub>2</sub> in N<sub>2</sub> at atmospheric pressure. The surface coverage profiles along the catalyst length (Fig. 11b) at  $300^\circ\text{C}$  show that NH<sub>x</sub><sup>\*</sup> species are depleted close to the entrance, while NO<sub>2</sub><sup>\*</sup> is produced. Most of the surface (~90%) is covered with O<sup>\*</sup> (not shown). RPA in Fig. 11c shows that NH<sub>3</sub><sup>\*</sup> is sequentially oxidized to N<sup>\*</sup> via reactions R<sub>55</sub>:  $\text{NH}_3^* + \text{O}^* \rightarrow \text{NH}_2^* + \text{OH}^*$ , R<sub>58</sub>:  $\text{NH}_2^* + \text{O}^* \rightarrow \text{NH}^* + \text{OH}^*$ , R<sub>53</sub>:  $\text{NH}^* + * \rightarrow \text{N}^* + \text{H}^*$ , and R<sub>60</sub>:  $\text{NH}^* + \text{O}^* \rightarrow \text{N}^* + \text{OH}^*$ . The alternate path for NH<sup>\*</sup> oxidation is via R<sub>76</sub>:  $\text{NH}^* + \text{O}^* \rightarrow \text{NO}^* + \text{H}^*$  to form NO<sup>\*</sup>. This is consistent with the work of Bradley et al. [102], who suggested that the oxidation of NH intermediate could lead to the formation of NO and N<sub>2</sub>. N<sup>\*</sup> formed in reactions R<sub>60</sub> and R<sub>53</sub> desorbs as N<sub>2</sub>, whereas

NO<sup>\*</sup> formed in reaction R<sub>76</sub> further oxidizes through reaction R<sub>80</sub>:  $\text{NO}^* + \text{O}^* \rightarrow \text{NO}_2^* + *$ . Most of the NO<sub>2</sub><sup>\*</sup> desorbs, but some of it is converted back to NO<sup>\*</sup> through reaction R<sub>78</sub>:  $\text{NO}_2^* + \text{H}^* \rightarrow \text{NO}^* + \text{OH}^*$ . RPA at  $275^\circ\text{C}$  shows that the H<sub>2</sub>O originates from reactions R<sub>62</sub>:  $\text{NH}_3^* + \text{OH}^* \rightarrow \text{NH}_2^* + \text{H}_2\text{O}^*$ , R<sub>64</sub>:  $\text{NH}_2^* + \text{OH}^* \rightarrow \text{NH}^* + \text{H}_2\text{O}^*$ , R<sub>24</sub>:  $2\text{OH}^* \rightarrow \text{H}_2\text{O}^* + \text{O}^*$ , and R<sub>22</sub>:  $\text{H}^* + \text{OH}^* \rightarrow \text{H}_2\text{O}^* + *$ .

With a minor adjustment of only one bond index for reaction pair R<sub>59</sub>-R<sub>60</sub>:  $\text{N}^* + \text{OH}^* \rightarrow \text{NH}^* + \text{O}^*$  from 0.5 to 0.6, the model is able to capture the experimental data over the entire temperature range. We note that this bond index was earlier set to 0.65 in the TPR analysis presented in Section 3.2.4. Even though the UHV-TPR experiments conducted on single crystal surfaces typically provide decent initial estimates of kinetic parameters, some further refinement is typically necessary to capture the practically more relevant atmospheric pressure data on polycrystalline or supported catalysts (this again points to the pressure and materials gap).

### 4.5. HCN oxidation

The final comparison for model predictions vs. experimental data is for HCN oxidation on Pt, as shown in Fig. 12a. The experimental data is taken from fixed bed reactor experiments conducted with 30 ppm of HCN and 6% O<sub>2</sub> on a Pt/Al<sub>2</sub>O<sub>3</sub> catalyst [11]. The support and catalyst details are as follows [11]: Pt/Al<sub>2</sub>O<sub>3</sub> pellet catalyst (cylindrical extrudates), catalyst volume =  $2 \text{ cm}^3$ , pellet length = 0.13 inch, pellet diameter = 0.13 inch, Pt loading = 0.5%, and catalyst weight = 2.1 g. Axial surface coverage profiles at  $225^\circ\text{C}$  (Fig. 12b) show that HCN<sup>\*</sup> decreases along the catalyst length, while NO<sub>2</sub><sup>\*</sup> increases. Similar to NH<sub>3</sub> oxidation, most of the surface (~97%) is covered with O<sup>\*</sup> (not shown). RPA, shown in Fig. 12c, indicates that under these operating conditions, HCN oxidation path via reaction R<sub>87</sub>:  $\text{HCN}^* + \text{O}^* \rightarrow \text{CN}^* + \text{OH}^*$  dominates the alternative path of HCN decomposition via reaction R<sub>85</sub>:  $\text{HCN}^* + * \rightarrow \text{H}^* + \text{CN}^*$ .

We have adjusted the bond index of reaction pair R<sub>87</sub>-R<sub>88</sub> from 0.5 to 0.7 to capture the low temperature HCN conversion data. We note that this bond index was earlier set to 0.44 in the TPR analysis presented in Section 3.2.5. As mentioned earlier, some parameter refinement is generally required for the transition from UHV simulations to practically more relevant atmospheric pressure simulations on polycrystalline or supported catalysts. Once CN<sup>\*</sup> is formed, it is oxidized via two major pathways, viz., reactions R<sub>91</sub>:  $\text{CN}^* + \text{O}^* \rightarrow \text{C}^* + \text{NO}^*$  and R<sub>94</sub>:  $\text{CN}^* + \text{O}^* \leftrightarrow \text{CO}^* + \text{N}^*$ , producing NO<sup>\*</sup> and N<sup>\*</sup>, respectively. Bond indices of these two reaction pairs (R<sub>91</sub>-R<sub>92</sub> and R<sub>93</sub>-R<sub>94</sub>) are modified from 0.5 to 0.3 and 0.7, respectively, to facilitate NO<sup>\*</sup> formation and subsequent oxidation to NO<sub>2</sub> and N<sub>2</sub>O, which were reported as oxidation products by Zhao et al. in their experiments [11]. Binding energy of HCN was slightly adjusted to 21.3 kcal/mol ( $Q_{\text{HCN}}^{\text{TPD}} = 26.1 \text{ kcal/mol}$ ,  $Q_{\text{HCN}}^{\text{avg}} = 21.4 \text{ kcal/mol}$  from Table 2, literature range 14–30 kcal/mol [53,68]) to capture the experimental data. Our HCN oxidation reaction mechanism shows good agreement with the experimental data, albeit with some parameter modification. In general, the HCN oxidation experiments are rare in literature, due to its high toxicity and lethal nature. Additional validation of this reaction mechanism will be carried out in the future, as more data becomes available for HCN oxidation under practically relevant operating conditions.

## 5. Preliminary mechanism reduction

Based on RPA, some reactions in the detailed surface reaction mechanism are identified as the least important ones. These include the adsorption/desorption steps for radicals, viz., H, O, OH, COOH, HCO, N, NH, NH<sub>2</sub>, C, and CN, as these species are more dominant on the catalyst surface than in the gas phase. Based on the HCN-TPD

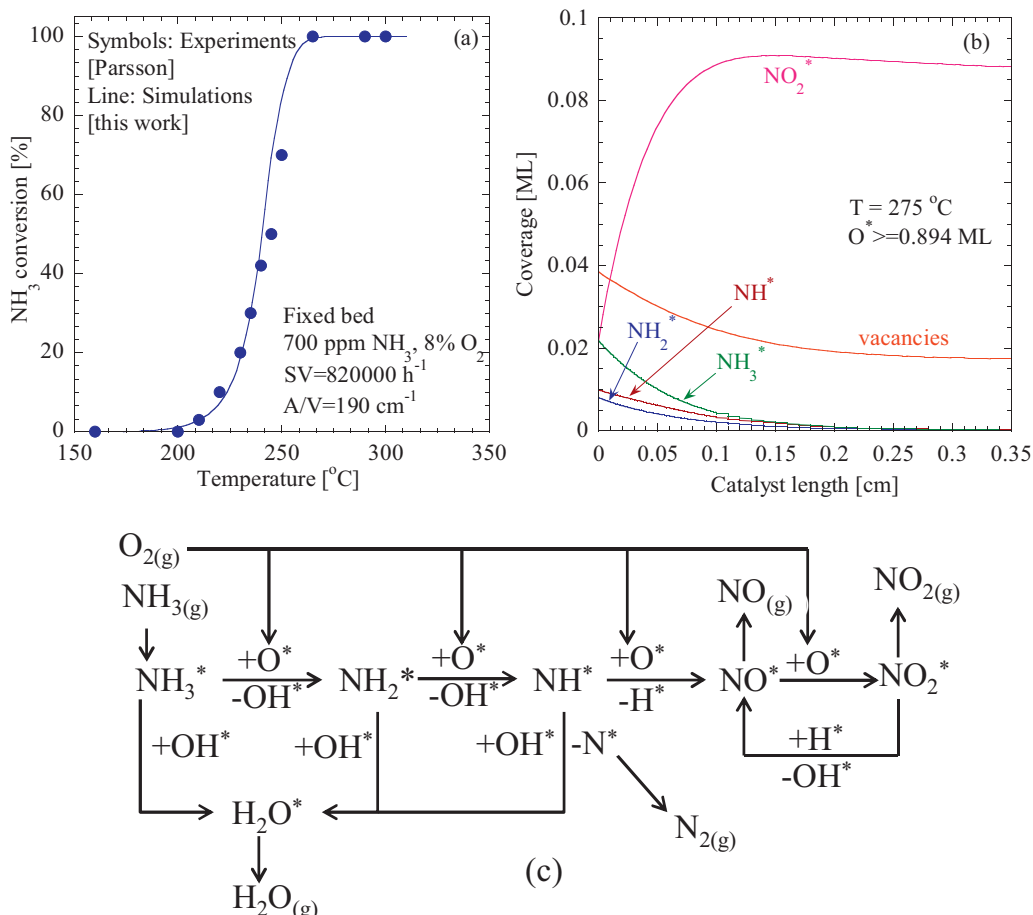


**Fig. 11.** Performance (panel a) and analysis (panels b and c) of the microkinetic model for  $\text{NH}_3$  oxidation on  $\text{Pt}/\text{Al}_2\text{O}_3$  fixed bed. Symbols represent the experimental data, whereas lines represent our simulations. Panel b shows the coverage profiles of dominant surface species ( $\text{O}^* \sim 90\%$ , not shown) along the catalyst length at  $275 \text{ }^{\circ}\text{C}$ . Panel c shows the dominant reaction pathways in the  $\text{NH}_3$  oxidation chemistry at  $275 \text{ }^{\circ}\text{C}$  (at the entrance of the catalyst). Operating conditions:  $\text{Pt}/\text{Al}_2\text{O}_3$  fixed bed reactor [101]; feed of 300 ppm  $\text{NH}_3$ , 6%  $\text{O}_2$ , and  $\sim 94\%$   $\text{N}_2$ ; space velocity of  $820,000 \text{ h}^{-1}$ ; and catalyst area per unit reactor volume of  $190 \text{ cm}^{-1}$ . Simulations are in close agreement with the experimental data.

(Section 3.1) and HCN-TPR (Section 3.2.5) simulations, the  $\text{C}_2\text{N}_2$  adsorption/desorption and formation/decomposition chemistry is important only at high temperatures ( $\sim 700 \text{ K}$ ); therefore, it can be ignored from the simulations at typical DOC conditions. Finally, some of the reactions in the  $\text{COOH}^*$  chemistry (e.g., reactions of  $\text{COOH}^*$  with  $\text{H}^*$ ,  $\text{O}^*$ , and  $\text{OH}^*$ ) are found to be less important than its formation from  $\text{CO}^* + \text{OH}^*$  and its decomposition to  $\text{CO}_2^* + \text{H}^*$ . This preliminary model reduction results in a shorter surface reaction mechanism with 94 steps (47 reversible) and 20 surface species. The unimportant reactions are listed in Appendix A (Table S1) (shaded reactions in the second column).

## 6. Limitations of the overall approach

To our knowledge, the reaction mechanism presented in this work is the first comprehensive microkinetic model that simultaneously captures five major emissions oxidation chemistries on Pt under UHV as well as practically more relevant operating conditions. Nonetheless, it is important to acknowledge the key limitations of the overall approach along with the future work needed to improve the mechanism presented here.

### 6.1. Limitations associated with the reaction mechanism and the uncertainty in kinetic parameters

- Current work focuses on the oxidation of five emissions ( $\text{CO}$ ,  $\text{NO}$ ,  $\text{CH}_2\text{O}$ ,  $\text{NH}_3$ , and HCN) only. These species contain only 1C and/or N

atom. After HC-SCR, the exhaust can contain additional secondary emissions, such as non-methane hydrocarbons ( $\text{C}_2\text{H}_4$ ), aldehydes ( $\text{CH}_3\text{CHO}$ ), and nitrogen-containing species ( $\text{CH}_3\text{CN}$ ). The emissions oxidation mechanism should be expanded to include such species with more C atoms.

- Beyond the C- and N-containing species, the exhaust also contains S-species, such as  $\text{SO}_2$ , which originate from the oxidation of sulfur in the diesel fuel.  $\text{SO}_2$  can be oxidized on the DOC to  $\text{SO}_3$ , which in turn could be hydrated (due to the steam in the exhaust) to sulfuric acid. Both, metal and support in the DOC, can interact with the sulfur oxides and sulfuric acid, resulting in catalyst deactivation due to sulfation [15,103,104]. The Schneider research group has conducted significant work in sulfur oxide chemistry on Pt using DFT [105–108]. Future work should include such chemistry in the emissions oxidation mechanism.
- Uncertainty in the kinetic parameters originates from the use of various estimation methods and their accuracy. For example, species binding energies and adsorbate-adsorbate interactions estimated using the UHV-TPD experiments can vary to some extent among different experiments. Activation energies for the surface reactions are calculated using the semi-empirical UBI-QEP method [37]. Even though the UBI-QEP method is highly convenient in accounting for coverage effects and ensuring enthalpic consistency, the calculated activation energies need to be verified with first-principles DFT calculations. A number of bond indices are modified in this work to improve the agreement

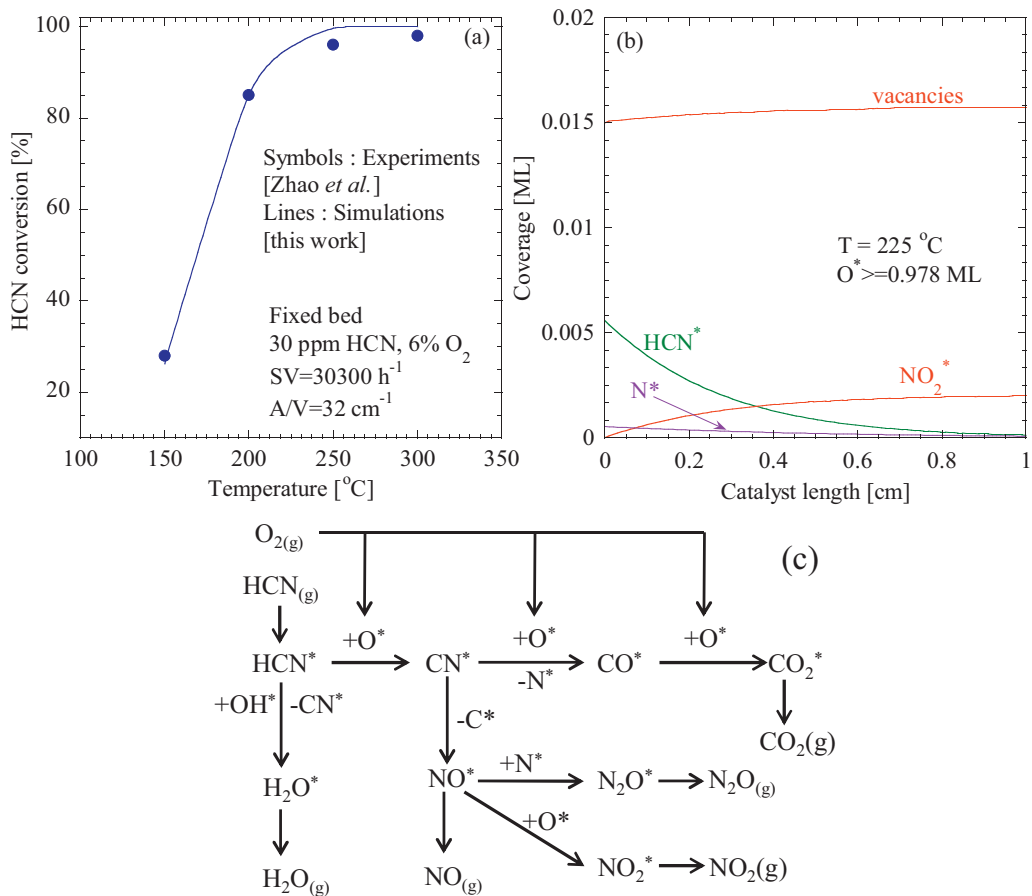


**Fig. 12.** Performance (panel a) and analysis (panels b and c) of the microkinetic model for HCN oxidation on Pt fixed bed. Symbols represent the experimental data, whereas lines represent our simulations. Panel b shows the coverage profiles of dominant surface species ( $O^* \sim 97\%$ , not shown) along the catalyst length at  $225\text{ }^\circ\text{C}$ . Panel c shows the dominant reaction pathways in the HCN oxidation chemistry at  $225\text{ }^\circ\text{C}$  (at the entrance of the catalyst). Operating conditions: Pt/Al<sub>2</sub>O<sub>3</sub> fixed bed reactor [11]; feed of 30 ppm HCN, 6% O<sub>2</sub>, and  $\sim 94\%$  N<sub>2</sub>; space velocity of  $30,300\text{ h}^{-1}$ ; and catalyst area per unit reactor volume of  $32\text{ cm}^{-1}$ . Simulations are in close agreement with the experimental data.

with the experimental data. Agreement between the UBI-QEP and DFT values can be improved by adjusting the bond indices [109]. However, accurate estimates of activation energies and location of transition state along the reaction coordinate are needed to verify the modifications conducted here. Finally, uncertainty in the experimental measurements (if any) may be translated to the surface reaction mechanism through the adjustment of kinetic parameters.

- The reaction mechanism proposed here utilizes a single temperature exponent to account for equilibrium limitations of NO oxidation in the considered temperature range. As all reactions are theoretically reversible, temperature exponents could be considered for the entire reaction mechanism, consistent with the approaches presented in literature [96,110–112]. However, out of the five emissions oxidation chemistries studied here, only NO oxidation is reversible in the considered temperature range, whereas all other reactions are practically irreversible. Presence of a large amount of O<sub>2</sub> ( $\sim 10\text{--}15\%$ ) in the diesel exhaust compared to the dilute levels of emissions also drives most of the emissions oxidation reactions toward the oxidized products. To ensure simplicity and practical applicability of the reaction mechanism, we have chosen to include only a single temperature exponent that is necessary for capturing the equilibrium limitations for NO oxidation.

- The mechanism reduction presented here is preliminary compared to more rigorous approaches based on principal component analysis and small parameter asymptotics [113,114].

## 6.2. Limitations associated with the catalyst and reactor modeling

- Catalyst site density used in the simulations ( $1.5 \times 10^{15}\text{ sites/cm}^2$ ) is calculated from Pt(1 1 1), which is one of the most stable facets of the Pt crystal. However, the actually utilized catalysts are polycrystalline in nature. Multiple types of sites and facets—which may be relevant to the real-life catalyst operation—are not taken into account. Active site density could vary with the catalyst loading, type of support, and catalyst life (deactivation/poisoning); however these effects are not considered in this work.
- Catalyst supports, such as ceria and zirconia, can play an active role in the emissions oxidation kinetics along with Pt. This work primarily focuses on relatively inert supports, such as alumina and titania. Nonetheless, our simplified approach for microkinetic modeling on Pt does not account for the role of support in emissions oxidation kinetics.
- A steady state isothermal PFR model is employed in the simulations. The assumption about isothermality is based on the very small amount of heat generated during the oxidation of dilute concentration levels for the emissions components. Future work will focus on investigating the performance of emissions oxidation mechanism under transient operating conditions for an exhaust containing multiple emissions.

## 7. Conclusions

In this paper, we have reported the first microkinetic model for the oxidation of five major emissions (CO, NO, CH<sub>2</sub>O, NH<sub>3</sub>,

and HCN) on a Pt-based DOC. The comprehensive microkinetic model contains 124 irreversible (62 reversible) steps and 21 surface species (94 steps and 20 species for the reduced version). Kinetic parameters are extracted using multiple techniques, such as the semi-empirical UBI-QEP method, literature DFT calculations, and simulations of various UHV temperature programmed experiments (TPD/TPR). Parameters extracted/estimated from such techniques are very good initial estimates, but they still require some adjustment to capture and predict the experimental data at practically more relevant operating conditions (atmospheric pressure, high O<sub>2</sub> concentration, dilute level of emissions, high space velocity, monolith- or powder-scale setups, etc.). The microkinetic model shows very good agreement with various sets of experimental data focused on emissions oxidation. The surface reaction mechanism developed in this work provides an excellent starting point for DOC design and optimization, and could be further expanded by including the chemistry of additional C<sub>2</sub>-C<sub>3</sub> species and sulfur impurities in the exhaust.

## Acknowledgments

H.N.S. acknowledges Department of Education GAANN Fellowship for funding support. The authors thank Prof. Pu-Xian Gao (UConn) for providing Pt/ZnO monolith samples for the CO oxidation tests.

## Appendix A. Supplementary data

Supplementary data associated with this article can be found, in the online version, at <http://dx.doi.org/10.1016/j.apcatb.2012.08.021>.

References [29,34,53,59,65,83,88,110,115–126] in Table S1 in the supplementary material correspond to the main text.

## References

- [1] B. Dudley, BP statistical review of world energy. <http://www.bp.com/sectionbodycopy.do?categoryId=7500&contentId=7068481>, 2011 (accessed June 30, 2011).
- [2] Petroleum watch, [http://energyalmanac.ca.gov/petroleum/petroleum.watch/2011-09-16\\_Petroleum\\_Watch.pdf](http://energyalmanac.ca.gov/petroleum/petroleum.watch/2011-09-16_Petroleum_Watch.pdf), 2011 (accessed Feb 05, 2012).
- [3] Diesel powers the US economy, <http://www.dieselforum.org/files/dmfile/FINALWebPDFVersion-NoAppendices.pdf>, 2011 (accessed June 01, 2012).
- [4] Problems of diesel, <http://www.catf.us/diesel/problems>, 2011 (accessed March 09, 2012).
- [5] Schneider, C.G.; Hill, L.B. Diesel and Health in America: The Lingering Threat; Clean Air Task Force: Boston, MA, [http://www.catf.us/resources/publications/files/Diesel\\_Health\\_in\\_America.pdf](http://www.catf.us/resources/publications/files/Diesel_Health_in_America.pdf), 2005 (accessed May 25, 2012).
- [6] P. Bera, M.S. Hegde, Journal of the Indian Institute of Science 90 (2010) 299–325.
- [7] M.C.H. Lim, G.A. Ayoko, L. Morawska, Z.D. Ristovski, E. Rohan Jayaratne, Atmospheric Environment 39 (2005) 7836–7848.
- [8] H. Chiang, Y. Lai, S. Chang, Atmospheric Environment 47 (2012) 399–406.
- [9] R. Prasad, V.R. Bella, Bulletin of Chemical Reaction Engineering and Catalysis 5 (2010) 69–86.
- [10] O. Kröcher, M. Elsener, Applied Catalysis B- Environmental 92 (2009) 75–89.
- [11] H. Zhao, R.G. Tonkyn, S.E. Barlow, B.E. Koel, C.H.F. Peden, Applied Catalysis B- Environmental 65 (2006) 282–290.
- [12] Emission standards, <http://www.dieselnet.com/standards/eu/hd.php>, 2011 (accessed Feb 05, 2012).
- [13] A. Macor, F. Avella, D. Faedo, Applied Energy 88 (2011) 4989–5001.
- [14] P. Tan, Z. Hu, D. Lou, Fuel 88 (2009) 1086–1091.
- [15] J. Luo, D. Kisinger, A. Abedi, W.S. Epling, Applied Catalysis A-General 383 (2010) 182–191.
- [16] A. Russell, W.S. Epling, Catalysis Reviews 53 (2011) 337–423.
- [17] M. Koebel, G. Madia, M. Elsener, Catalysis Today 73 (2002) 239–247.
- [18] A. Setiabudi, M. Makkee, J.A. Moulijn, Applied Catalysis B- Environmental 50 (2004) 185–194.
- [19] C.J. Tighe, M.V. Twigg, A.N. Hayhurst, J.S. Dennis, Combustion and Flame 159 (2012) 77–90.
- [20] M. Shrivastava, A. Nguyen, Z. Zheng, H. Wu, H.S. Jung, Environmental Science Technology 44 (2010) 4796–4801.
- [21] Reciprocating engines, <http://www.poweronsite.org/AppGuide/Chapters/Chap4/4-1.Recip.Engines.htm#Introduction>, 2012 (accessed April 2, 2012).
- [22] Stationary gas turbines, <http://www.epa.gov/ttnchie1/ap42/ch03/final/c03s01.pdf>, 2012 (accessed April 2, 2012).
- [23] Emission control system: Stationary catalytic converter, <http://www.wardcleanairproducts.com/Stationary-Catalytic-Converters/quick-lid-for-stationary-engines-above-700hp.html>, 2012 (accessed April 4, 2012).
- [24] S. Salomons, PhD thesis, University of Alberta, Alberta, Canada (2008) 1–277.
- [25] J.L. Gland, E.B. Kollin, Journal of Chemical Physics 78 (1983) 963–974.
- [26] A.L. Gerrard, J.F. Weaver, Journal of Chemical Physics 123 (2005) 224703.
- [27] A.S. Ivanova, E.M. Slavinskaya, R.V. Gulyaev, V.I. Zaikovskii, O.A. Stonkus, I.G. Danilova, et al., Applied Catalysis B- Environmental 97 (2010) 57–71.
- [28] A. Manasila, E. Gulari, Applied Catalysis B- Environmental 37 (2002) 17–25.
- [29] A.B. Mhadeshwar, D.G. Vlachos, Combustion and Flame 142 (2005) 289–298.
- [30] N. Rankovic, A. Nicolle, P. Da Costa, Journal of Physical Chemistry C 114 (2010) 7102–7111.
- [31] N. Rankovic, A. Nicolle, D. Berthout, P. Da Costa, Catalysis Communication 12 (2010) 54–57.
- [32] M. Crocoll, S. Kureti, W. Weisweiler, Journal of Catalysis 229 (2005) 480–489.
- [33] L. Olsson, H. Persson, E. Fridell, M. Skoglundh, B. Andersson, Journal of Physical Chemistry B 105 (2001) 6895–6906.
- [34] W. Hauptmann, M. Votsmeier, J. Gieshoff, D. Vlachos, A. Drochner, H. Vogel, Topics in Catalysis 52 (2009) 1925–1928.
- [35] R.J. Gorte, J.L. Gland, Surface Science 102 (1981) 348–358.
- [36] N. Rankovic, A. Nicolle, D. Berthout, P. Da Costa, Journal of Physical Chemistry C 115 (2011) 20225–20236.
- [37] E. Shustorovich, H. Sellers, Surface Science Reports 31 (1998) 1–119.
- [38] E. Shustorovich, Advances in Catalysis 37 (1990) 101–164.
- [39] J.A. Dumesic, D.F. Rudd, L.M. Aparicio, J.E. Rekoske, A.A. Trevino, The Microkinetics of Heterogeneous Catalysis, 1st Ed., American Chemical Society, 1993.
- [40] R.J. Gorte, L.D. Schmidt, J.L. Gland, Surface Science 109 (1981) 367–380.
- [41] G.P. Smith, D.M. Golden, M. Frenklach, N.W. Moriarty, B. Eteneer, M. Goldenberg, et al., GRI-Mech 3.0, <http://www.me.berkeley.edu/gri.mech/>, 1999 (accessed Nov 1, 2011).
- [42] N.K. Ray, A.B. Anderson, Surface Science 119 (1982) 35–45.
- [43] Y. Ishikawa, M. Liao, C.R. Cabrera, Surface Science 463 (2000) 66–80.
- [44] C. Daniel, M.O. Clarté, S.P. Teh, O. Thinon, H. Provendier, A.C. Van Veen, et al., Journal of Catalysis 272 (2010) 55–64.
- [45] M. Rinnemo, D. Kulginov, S. Johansson, K.L. Wong, V.P. Zhdanov, B. Kasemo, Surface Science 376 (1997) 297–309.
- [46] M. Lynch, P. Hu, Surface Science 458 (2000) 1–14.
- [47] M. Stamatakis, Y. Chen, D.G. Vlachos, Journal of Physical Chemistry C 115 (2011) 24750–24762.
- [48] R.B. Getman, W.F. Schneider, ChemCatChem 2 (2010) 1450–1460.
- [49] W.S. Epling, L.E. Campbell, A. Yezerets, N.W. Currier, J.E. Parks, Catalysis Reviews 46 (2004) 163–245.
- [50] E.V. Rebrov, M.H.J.M. de Croon, J.C. Schouten, Chemical Engineering Journal 90 (2002) 61–76.
- [51] A. Scheuer, M. Votsmeier, A. Schuler, J. Gieshoff, A. Drochner, H. Vogel, Topics in Catalysis 52 (2009) 1847–1851.
- [52] J.L. Gland, Surface Science 71 (1978) 327–350.
- [53] D.C. Ford, Y. Xu, M. Mavrikakis, Surface Science 587 (2005) 159–174.
- [54] G. Novell-Leruth, PhD thesis, Universitat Rovira I Virgili, Tarragona, Spain (2009).
- [55] G. Novell-Leruth, A. Valcárcel, J. Pérez-Ramírez, J.M. Ricart, Journal of Physical Chemistry C 111 (2007) 860–868.
- [56] G. Novell-Leruth, J.M. Ricart, J. Pérez-Ramírez, Journal of Physical Chemistry C 112 (2008) 13554–13562.
- [57] F. Gobal, S. Azizian, Langmuir 13 (1997) 5999–6000.
- [58] M.E. Bartram, R.G. Windham, B.E. Koel, Langmuir 4 (1988) 240–246.
- [59] D. Mei, J. Du, M. Neurock, Industrial and Engineering Chemistry Research 49 (2010) 10364–10373.
- [60] M.E. Bartram, R.G. Windham, B.E. Koel, Surface Science 184 (1987) 57–74.
- [61] R.B. Getman, W.F. Schneider, Journal of Physical Chemistry C 111 (2007) 389–397.
- [62] S. Ovesson, B.I. Lundqvist, W.F. Schneider, A. Bogicevic, Phys. Rev. B. 71 (2005) 115406-1–115406-5.
- [63] D. Mei, Q. Ge, M. Neurock, L. Kieken, J. Lerou, Molecular Physics 102 (2004) 361–369.
- [64] N.M. Abbas, R.J. Madix, Applied Surface Science 3 (1981) 241–275.
- [65] S.K. Desai, M. Neurock, K. Kourtakis, Journal of Physical Chemistry B 106 (2002) 2559–2568.
- [66] J. Greeley, M. Mavrikakis, Journal of American Chemical Society 126 (2004) 3910–3919.
- [67] P.L. Hagans, X. Guo, I. Chorkendorff, A. Winkler, H. Siddiqui, J.T. Yates Jr., Surface Science 203 (1988) 1–16.
- [68] E. Herceg, M. Trenary, Journal of Physical Chemistry B 109 (2005) 17560–17566.
- [69] C.L. Levoguer, R.M. Nix, Journal of the Chemical Society, Faraday Transactions 92 (1996) 4799–4807.
- [70] J.R. Kingsley, J.C. Hemminger, Surface Science 181 (1987) L156–L162.
- [71] J.M. Lindquist, J.P. Ziegler, J.C. Hemminger, Surface Science 210 (1989) 27–45.
- [72] J.R. Kingsley, J.C. Hemminger, Langmuir 2 (1986) 460–464.
- [73] K. Mudiyanselage, C. Yi, J. Szanyi, Journal of Physical Chemistry C 113 (2009) 5766–5776.
- [74] M.E. Bartram, B.E. Koel, E.A. Carter, Surface Science 219 (1989) 467–489.
- [75] W.D. Mieher, R.A. Pelak, W. Ho, Surface Science 359 (1996) 23–36.
- [76] G.A. Attard, H.D. Ebert, R. Parsons, Surface Science 240 (1990) 125–135.

[77] M.A. Henderson, G.E. Mitchell, J.M. White, *Surface Science* 188 (1987) 206–218.

[78] W.D. Mieher, W. Ho, *Surface Science* 322 (1995) 151–167.

[79] C. Panja, PhD thesis, University of Southern California, Los Angeles, California, USA (2000).

[80] G.B. Fisher, J.L. Gland, *Surface Science* 94 (1980) 446–455.

[81] W. Gao, J.A. Keith, J. Anton, T. Jacob, *Dalton Transactions* 39 (2010) 8450–8456.

[82] S. Alayoglu, A.U. Nilekar, M. Mavrikakis, B. Eichhorn, *Nature Materials* 7 (2008) 333–338.

[83] W.K. Offermans, A.P.J. Jansen, R.A. Van Santen, G. Novell-Leruth, J.M. Ricart, J. Pérez-Ramírez, *Journal of Physical Chemistry C* 111 (2007) 17551–17557.

[84] E. Shustorovich, A. Zeigarnik, *Russian Journal of Physical Chemistry A* 80 (2006) 4–30.

[85] W.K. Offermans, A.P.J. Jansen, R.A. van Santen, *Surface Science* 600 (2006) 1714–1734.

[86] X. Guo, A. Winkler, I. Chorkendorff, P.L. Hagans, H.R. Siddiqui, J.T. Yates Jr., *Surface Science* 203 (1988) 17–32.

[87] K. Arnby, A. Törncrona, B. Andersson, M. Skoglundh, *Journal of Catalysis* 221 (2004) 252–261.

[88] A.V. Myshlyavtsev, V.P. Zhdanov, *Langmuir* 9 (1993) 1290–1298.

[89] R.J.H. Grisel, J.J. Slyconish, B.E. Nieuwenhuys, *Topics in Catalysis* 16–17 (2001) 425–431.

[90] A. Bourane, D. Bianchi, *Journal of Catalysis* 209 (2002) 126–134.

[91] P. Carlsson, M. Skoglundh, *Applied Catalysis B- Environmental* 101 (2011) 669–675.

[92] BenchCAT reactor, <http://www.altamirainstruments.com/benchcat.html>, 2012 (accessed Feb 24, 2012).

[93] D. Bhatia, R.W. McCabe, M.P. Harold, V. Balakotaiah, *Journal of Catalysis* 266 (2009) 106–119.

[94] C. Morley, Gaseq, A chemical equilibrium program for windows, <http://www.c.morley.dsl.pipex.com>, 2005 (accessed April 06, 2012).

[95] R. Marques, P. Darcy, P.D. Costa, H. Mellottée, J. Trichard, G. Djéga-Mariadassou, *Journal of Molecular Catalysis A: Chemical* 221 (2004) 127–136.

[96] A.B. Mhadeshwar, H. Wang, D.G. Vlachos, *Journal of Physical Chemistry B* 107 (2003) 12721–12733.

[97] S. Appari, V.M. Janardhanan, S. Jayanti, L. Maier, S. Tischer, O. Deutschmann, *Chemical Engineering Science* 66 (2011) 5184–5191.

[98] C. Zhang, H. He, K. Tanaka, *Applied Catalysis B- Environmental* 65 (2006) 37–43.

[99] J. Peng, S. Wang, *Applied Catalysis B- Environmental* 73 (2007) 282–291.

[100] R.W. McCabe, D.F. McCready, *Chemical Physics Letters* 111 (1984) 89–93.

[101] H. Parsson, Selective catalytic oxidation of ammonia, <http://www.chemeng.lth.se/exjobb/044.pdf>, 2004 (accessed May 05, 2012).

[102] J.M. Bradley, A. Hopkinson, D.A. King, *Journal of Physical Chemistry* 99 (1995) 17032–17042.

[103] O. Kröcher, M. Widmer, M. Elsener, D. Rothe, *Industrial and Engineering Chemistry Research* 48 (2009) 9847–9857.

[104] T. Kollti, M. Huuhtanen, A. Hallikainen, K. Kallinen, R. Keiski, *Catalysis Letters* 127 (2009) 49–54.

[105] X. Lin, N.J. Ramer, A.M. Rappe, K.C. Hass, W.F. Schneider, B.L. Trout, *Journal of Physical Chemistry B* 105 (2001) 7739–7747.

[106] X. Lin, K.C. Hass, W.F. Schneider, B.L. Trout, *Journal of Physical Chemistry B* 106 (2002) 12575–12583.

[107] X. Lin, W.F. Schneider, B.L. Trout, *Journal of Physical Chemistry B* 108 (2004) 13329–13340.

[108] X. Lin, W.F. Schneider, B.L. Trout, *Journal of Physical Chemistry B* 108 (2004) 250–264.

[109] M. Maestri, K. Reuter, *Angewandte Chemie International Edition* 50 (2011) 1194–1197.

[110] A.B. Mhadeshwar, D.G. Vlachos, *Industrial and Engineering Chemistry Research* 46 (2007) 5310–5324.

[111] A.B. Mhadeshwar, D.G. Vlachos, *Journal of Physical Chemistry B* 109 (2005) 16819–16835.

[112] M. Maestri, D.G. Vlachos, A. Beretta, G. Groppi, E. Tronconi, *AIChE Journal* 55 (2009) 993–1008.

[113] A.B. Mhadeshwar, D.G. Vlachos, *Catalysis Today* 105 (2005) 162–172.

[114] M. Salciccioli, Y. Chen, D.G. Vlachos, *Industrial and Engineering Chemistry Research* 50 (2011) 28–40.

[115] L.C. Grabow, A.A. Gokhale, S.T. Evans, J.A. Dumesic, M. Mavrikakis, *Journal of Physical Chemistry C* 112 (2008) 4608–4617.

[116] C.T. Campbell, G. Ertl, H. Kuipers, J. Segner, *Surface Science* 107 (1981) 220–236.

[117] Y.Y. Yeo, L. Vattuone, D.A. King, *Journal of Chemical Physics* 106 (1997) 392–401.

[118] W. Hauptmann, M. Votsmeier, H. Vogel, D.G. Vlachos, *Applied Catalysis A-General* 397 (2011) 174–182.

[119] Y. Lin, J. Sun, J. Yi, J. Lin, H. Chen, D. Liao, *Journal of Molecular Structure - Theochemistry* 587 (2002) 63–71.

[120] G. Estiu, S.A. Maluendes, E.A. Castro, A.J. Arvia, *Journal of Physical Chemistry* 92 (1988) 2512–2516.

[121] J. Kua, W.A. Goddard III, *Journal of American Chemical Society* 121 (1999) 10928–10941.

[122] D.A. Hansgen, D.G. Vlachos, J.G. Chen, *Nature Chemistry* 2 (2010) 484–489.

[123] C.T. Campbell, G. Ertl, J. Segner, *Surface Science* 115 (1982) 309–322.

[124] A.A. Gokhale, S. Kandoi, J.P. Greeley, M. Mavrikakis, J.A. Dumesic, *Chemical Engineering Science* 59 (2004) 4679–4691.

[125] A. Michaelides, P. Hu, *Theoretical Aspects of Heterogeneous Catalysis*, Springer Netherlands, 2002, pp. 199–215.

[126] Y. Chen, D.G. Vlachos, *Journal of Physical Chemistry C* 114 (2010) 4973–4982.

[127] D.H. Parker, M.E. Bartram, B.E. Koel, *Surface Science* 217 (1989) 489–510.

[128] J.L. Gland, B.A. Sexton, G.B. Fisher, *Surface Science* 95 (1980) 587–602.

[129] V.P. Zhdanov, B. Kasemo, *Surface Science* 415 (1998) 403–410.

[130] J.F. Weaver, J. Chen, A.L. Gerrard, *Surface Science* 592 (2005) 83–103.

[131] M.T. Paffett, S.C. Gebhard, R.G. Windham, B.E. Koel, *Journal of Physical Chemistry* 94 (1990) 6831–6839.

[132] B.E. Hayden, A.M. Bradshaw, *Surface Science* 125 (1983) 787–802.

[133] S.C. Gebhard, B.E. Koel, *Journal of Physical Chemistry* 96 (1992) 7056–7063.

[134] T. Ichiiya, N. Koiwa, A. Ohma, S. Tada, K. Fushinobu, K. Okazaki, *Nanoscale and Microscale Thermophysical Engineering* 14 (2010) 110–122.

[135] H. Zhu, W. Guo, R. Jiang, L. Zhao, X. Lu, M. Li, et al., *Langmuir* 26 (2010) 12017–12025.

[136] D.C. Ford, A.U. Nilekar, Y. Xu, M. Mavrikakis, *Surface Science* 604 (2010) 1565–1575.

[137] R.W. McCabe, L.D. Schmidt, *Surface Science* 65 (1977) 189–209.

[138] Y. Zhai, D. Pierre, R. Si, W. Deng, P. Ferrin, A.U. Nilekar, et al., *Science* 329 (2010) 1633–1636.

[139] J. Meng, C.A. Menning, M.B. Zellner, J.G. Chen, *Surface Science* 604 (2010) 1845–1853.

[140] G. Psofogiannakis, PhD thesis, University of Ottawa, Ottawa, Canada (2007).

[141] A. Picolin, C. Busse, A. Redinger, M. Morgenstern, T. Michely, *Journal of Physical Chemistry C* 113 (2009) 691–697.

[142] J.M. Gohndrone, C.W. Olsen, A.L. Backman, T.R. Gow, E. Yagasaki, R.I. Masel, *Journal of Vacuum Science and Technology A* 7 (1989) 1986–1990.

[143] K. Rasim, M. Bobeth, W. Pompe, N. Seriani, *Journal of Molecular Catalysis A: Chemical* 325 (2010) 15–24.

[144] J.L. Gland, E.B. Kollin, *Surface Science* 104 (1981) 478–490.

[145] H. Ibach, S. Lehwald, *Surface Science* 76 (1978) 1–12.

[146] J.L. Gland, B.A. Sexton, *Surface Science* 94 (1980) 355–368.

[147] H. Celio, P. Mills, D. Jentz, Y.I. Pae, M. Trenary, *Langmuir* 14 (1998) 1379–1383.

[148] F.P. Netzer, *Surface Science* 61 (1976) 343–354.

[149] M.E. Bridge, R.M. Lambert, *Surface Science* 63 (1977) 315–324.